# Nature of vibrational excitations in vitreous silica

S. N. Taraskin and S. R. Elliott
*Department of Chemistry, University of Cambridge, Lensfield Road, Cambridge CB2 1EW, United Kingdom*
(Received 21 January 1997; revised manuscript received 22 May 1997)

The vibrational properties of models of vitreous silica constructed by molecular-dynamics simulation with different interatomic potentials have been investigated. The static and dynamical structure factors of the model systems are in good agreement with experimental data. Partial and total vibrational densities of states are presented. The characteristics of vibrational modes in different frequency ranges are investigated using a mode-projection technique. [S0163-1829(97)05737-8]

## I. INTRODUCTION

Vitreous silica is one of the principal network glass-forming systems and exhibits all the features that are typical of disordered materials. For instance, the medium-range order (MRO) of vitreous silica has been revealed by diffraction experiments;[1,2] e.g., pseudoperiodicity with a scale of $2\pi/Q_1 \simeq 4.1$ Å is associated with the position of the first sharp diffraction peak (FSDP) at $Q_1 \simeq 1.6$ Å$^{-1}$.[3] Excess vibrational modes, called the boson peak (BP), have been observed in Raman[4] and inelastic neutron[5] scattering, and IR absorption[6] in the low-frequency range $\sim 1$ THz. Low-temperature anomalies in thermodynamical properties are exhibited by vitreous silica as well.[7,8] A hump around $T \sim 10$–$30$ K in the temperature dependence of the reduced heat capacity, $C_v/T^3$ vs $T$, is associated with excess low-frequency vibrational modes in the BP region.[7] Very-low-temperature anomalies at $T \lesssim 1$ K, e.g., a linear temperature dependence of heat capacity, are probably connected with excitations of two-level systems.[9,10]

A few theoretical, mainly computational, studies of the problem of the vibrational behavior of vitreous silica and its crystalline counterparts (different polymorphs of $SiO_2$) have been performed.[11–24,26] The first step is the construction of a structural model of $v$-$SiO_2$; the simplest model, a handmade random network cluster, was constructed by Bell and Dean.[11] Later, more sophisticated computer-simulation-based structural models were created. The quality of these computer-simulated models depends crucially on the choice of interatomic potential. The very first simulations based on valence-force-field potentials took only the valence part of the interatomic interactions into consideration;[12–16] the ionic part was included later.[17,18] Structural models of crystalline polymorphs of $SiO_2$ and $v$-$SiO_2$ (modeled by a Bethe lattice[17,19]) based on these potentials were constructed by energy minimization. Two-body and three-body empirical interatomic potentials were developed and implemented in molecular-dynamics (MD) simulations.[20–25]. The polarizable ion model has been used to describe IR absorption in $v$-$SiO_2$.[26] A breakthrough was made by Tsuneyuki *et al.* who derived a pairwise potential from *ab initio* calculations, which was subsequently implemented in MD simulations of crystalline[27,28] and vitreous[29–31] $SiO_2$. An improved *ab initio*–based semiempirical pairwise potential was subsequently obtained[32] and used in a MD simulation of $v$-$SiO_2$.[33–35] *Ab initio* (Car-Parinello) MD simulation is the best technique for creating realistic structural models, although at present it is limited to small atomic structures; e.g., a model of $v$-$SiO_2$ containing 72 atoms was created using this approach.[36,37]

Vibrational analyses of $SiO_2$ models have been performed by diagonalizing the dynamical matrices calculated for crystalline[12,16–18,38] and vitreous[14,24,34,37] structural models, by the equation-of-motion technique,[39] and by calculating the velocity-velocity autocorrelation function.[20,23,29,30,40] By direct diagonalization of the dynamical matrix, Jin *et al.*[24] calculated the vibrational density of states (VDOS) of a structural model of vitreous silica based on a three-body empirical interatomic potential. The vibrational spectrum thus obtained reproduced the experimental data in the low- and intermediate-frequency regions reasonably well, but the peak splitting at around 35 THz in the high-frequency optic band was not found. Moreover, the structural model of $v$-$SiO_2$ constructed in Ref. 24 contains an unrealistically high concentration of coordination defects (dangling bonds and overcoordinated atoms). Della Valle and Venutti *et al.*[30] obtained the VDOS of $v$-$SiO_2$ from the velocity-velocity autocorrelation function for a structural model based on the Tsuneyuki potential. The influence of the rate of the quench on the shape of the VDOS has been investigated in Ref. 33 using the van Beest potential.[32] In the high-frequency region, use of the Tsuneyuki potential was found to result in a shift of the vibrational spectrum to lower frequencies compared with experiment. Quite a good comparison with the experimental VDOS has been achieved for the first-principles model of $v$-$SiO_2$.[37]

Mode-assignment analyses have been successfully made for crystalline silica polymorphs.[12,17,18] In vitreous silica, the mode-projection technique has been used to analyze the role of normal vibrations of some structural units ($SiO_2$ and $SiO_4$) in different frequency ranges for a Bethe-lattice model,[19] for a structural model with an empirical interatomic potential acounting for polarization effects,[26] and for an *ab initio* MD-constructed model.[37] It has been shown in Refs. 26 and 37 that the peaks at 37 THz and 32 THz in the high-frequency band can be associated with symmetric and asymmetric vibrations of $SiO_4$ structural units, respectively. The VDOS of an $SiO_4$ unit immersed in a silica matrix ob-

 

tained with the Tsuneyuki potential has been calculated in Ref. 31.

In our MD simulation, we have used the best available *ab initio*–based semiempirical pairwise interatomic potential due to van Beest *et al.*[32] used to describe the properties of different silica polymorphs. The Tsuneyuki potential[27] was also implemented for comparison. All the structural models that we have constructed are free of any coordination defects and show good agreement with experimental diffraction data.[34] The vibrational analysis was performed by direct diagonalization of the dynamical matrix.

The structure of the paper is the following. Section II describes details of the computer simulation. Characteristics of the static structure are analyzed in Sec. III. Dynamical properties of models of vitreous silica are considered in Sec. IV. In Sec. V, a mode analysis is performed. Conclusions are given in Sec. VI.

## II. DETAILS OF SIMULATIONS

We have simulated vitreous $SiO_2$ by a model containing 216 silicon and 432 oxygen atoms within a simulation cube of side length $L \simeq 21.39$ Å (with a density $\rho \simeq 2.2$ g/cm$^3$). A set of MD runs using the package DLPOLY (Ref. 41) (NVE, cubic periodic boundary conditions) with time step $=1$ fs was performed at different fixed temperatures. The temperature of the system was adjusted by velocity rescaling every 10 fs, making the time scale smaller than the minimum typical inverse vibrational frequency 1/40 THz$^{-1} = 25$ fs.

The Coulomb interactions were calculated using the Ewald summation method. Real and reciprocal space cutoffs were $\alpha^{-1} = 0.31$ Å$^{-1}$ and $k_{\max} \simeq 2.03$ Å$^{-1}$, respectively, and the pair interaction cutoff was $\simeq L/2$. At small interatomic distances (less than the average nearest-neighbor separation), the Tsuneyuki and the van Beest potentials have an energy barrier. However, the energy barrier is not high enough to prevent atoms from hopping over it at high temperatures and becoming coincident. We have therefore used modifications of the Tsuneyuki and van Beest potentials[42] which are free of this fault, due to the replacement of the energy barrier of finite height by an infinitely high potential wall. Both the Tsuneyuki and van Beest potentials have been modified by adding Lennard-Jones contributions [(18-6) and (24-6) terms, respectively; see Ref. 42 for more details] to the original interatomic potentials. At small interatomic distances the modified potentials go to infinity while at interatomic separations $\gtrsim 1.2$ Å for the Si-O interaction and $\gtrsim 1.8$ Å for the O-O interaction they practically coincide with the original potentials.

We started from the fluid state at $T = 5000$ K. At this temperature, significant diffusion takes place and the system has no memory of the initial valence network structure within a period of $\sim 50$ ps from the start of the simulation run. It was found that all valence bonds are broken, and all atoms change their nearest neighbors (previous connections can be reestablished only accidentally).

The temperature was gradually decreased by 100 K steps to $T \simeq 2000$ K with an average quench rate of $\simeq 10^{12}$ K/sec. This temperature quench resulted in a slowdown of diffusion accompanied by a related slowdown of bond-breaking kinetics. At the final temperature $T \simeq 2000$ K, atoms only vibrated around their equilibrium positions, and no diffusion occurred on the time scale of the MD run, $\sim 100$ ps. This temperature is somewhat higher than the glass-transition temperature in $v$-$SiO_2$, $T_g \simeq 1450$ K.[43] This known drawback can result both from deficiencies of the Tsuneyuki and van Beest potentials in describing the properties of liquid silica[42] and from the dependence of the glass-transition temperature on the quench rate[33] which is very far in the MD simulations from the experimental values ($\sim 10^2$ K/sec). Use of the more realistic $N$-$P$-$T$ ensemble with the same quench rate for the slightly modified van Beest potential results in a glass transition at $T_g \simeq 3150$ K [with density $\rho(T_g) = 2.35$ g/cm$^3$] and in a cessation of diffusion around $T \approx 1500$ K (a detailed discussion will be presented elsewhere). Subsequently, the system was relaxed to its equilibrium state at $T \lesssim 10^{-5}$ K by an effective MD energy-minimization run. Conjugate-gradient and steepest-descent methods were used to check that the system was in a ''glassy'' (metastable) energy minimum.

The dynamical matrix was calculated in the metastable glassy state and diagonalized directly. A complete set of eigenvalues and eigenvectors was used for subsequent vibrational analysis.

## III. STATIC-STRUCTURE CHARACTERISTICS

For a vibrational analysis, a high-quality structural model constructed by MD simulation is very important. The quality of the structural model strongly depends on the interatomic potential, and *ab initio* calculated potentials are the most reliable ones. Such a potential has been used in the MD simulation of small vitreous silica clusters (72 atoms) (Ref. 36) and their vibrational analysis.[37] We needed to study a larger system and therefore had to use the pairwise adaptation of many-particle interactions, e.g., the van Beest[32] and Tsuneyuki[27] potentials. Using these potentials, we obtained perfectly chemically bonded structural models of vitreous silica, free of any structural defects such as dangling bonds and overcoordinated atoms. The majority of the calculated data presented below are related (where it is not mentioned explicitly) to the system constructed with the van Beest potential, this being better representative of the vibrational properties of vitreous silica as compared to the Tsuneyuki potential.

### A. Radial and angle distribution functions

Partial radial distribution functions are important structural characteristics of amorphous structures. These functions have pronounced first peaks corresponding to the first coordination shell at the mean separation of atoms of different species (see Fig. 1). The positions of these peaks are at $d_{\text{Si-O}} = 1.613$ Å (1.61 Å), $d_{\text{O-O}} = 2.631$ Å (2.63 Å), and $d_{\text{Si-Si}} = 3.127$ Å (3.08 Å) which are in good agreement with the experimental values[44] given in brackets. The shape of the partial distribution functions is very similar to that obtained in Ref. 33 with the use of a cut-and-shifted van Beest potential.

The structure of vitreous silica consists of corner-shared tetrahedra ($SiO_4$ units). These units appear to be quite rigid because the average O-Si-O angle of 109.43° (see Fig. 2) is

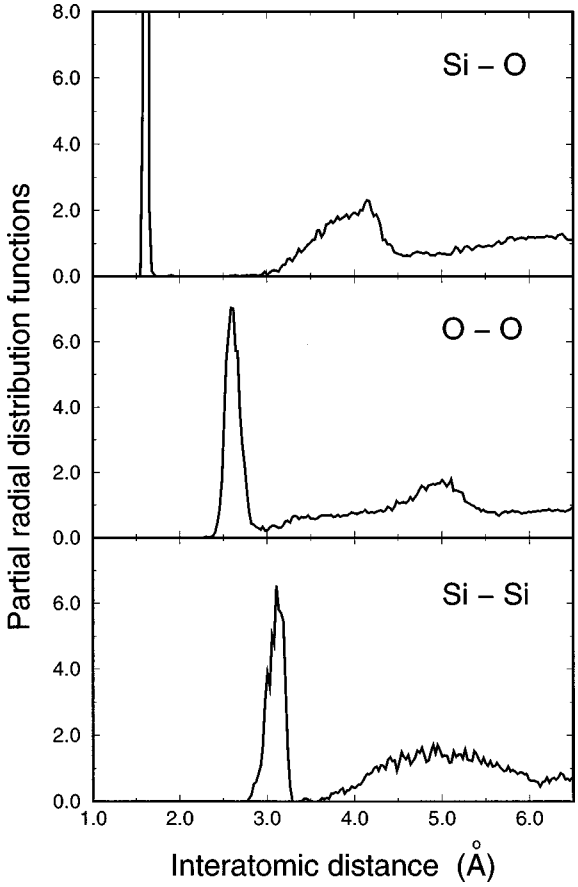


FIG. 1. Partial pair radial distribution functions vs interatomic distance for the relaxed structural model of $v$-$SiO_2$ constructed with use of the van Beest potential.

close to the ideal tetrahedral angle, 109.5°, and the distributions of Si-O and O-O distances are very narrow. A significant source of structural disorder in vitreous silica, therefore, as also mentioned in Ref. 36, is due to the comparatively wide Si-O-Si bridging-angle distribution, this being one of the most important structural characteristics. A comparison between the oxygen bond-angle distribution for vitreous silica obtained in our simulation using the van Beest potential and that found in x-ray and neutron diffraction experiments[45] is given in Fig. 2. The Si-O-Si angle distribution for our model is slightly broader in comparison with the experimental one and its maximum (around $\simeq 155°$, in accordance with results of Ref. 33) is shifted to a higher value relative to that for the experimental distribution (around $\simeq 142°$). However, the experimental Si-O-Si angle distributions measured by different techniques (including, e.g., NMR) do not coincide with each other and the maxima of these distributions lie in the range between 142° and 152° (see Ref. 45 for more details). The maxima of the distributions obtained for computer-constructed models are also quite different; e.g., the distribution for the Vashishta model has a maximum at 142°,[24] while *ab initio* MD simulations result in a maximum position around 130°.[36]

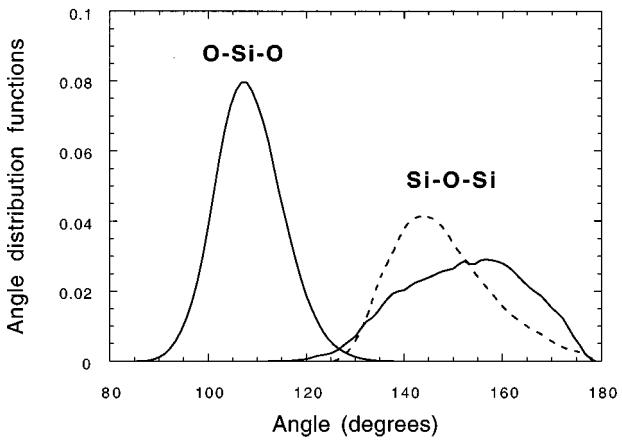


FIG. 2. Bond-angle Si-O-Si and O-Si-O distributions for our model constructed using the van Beest potential (the solid lines) and experimental data for the Si-O-Si distribution (Ref. 42) (the dashed line). The areas under both curves are normalized to unity.

### B. Static structure factor

Another important structural characteristic of amorphous solids is the static structure factor $S(\mathbf{Q})$, defined as[46]

$$S(\mathbf{Q})=1+\frac{1}{N\langle\overline{b^2}\rangle}\sum_{i\neq i'}\overline{b_i b_{i'}}e^{-W_{ii'}}e^{i\mathbf{Q}\cdot(\mathbf{R}_i-\mathbf{R}_{i'})}, \tag{1}$$

with the Debye-Waller term being given by

$$W_{ii'}=\frac{\hbar Q^2}{6}\sum_j\left(\frac{\mathbf{e}_i^j}{\sqrt{m_i}}-\frac{\mathbf{e}_{i'}^j}{\sqrt{m_{i'}}}\right)^2\frac{\overline{n_j}+1/2}{\omega_j}, \tag{2}$$

where $\langle\overline{b^2}\rangle=N^{-1}\Sigma_i\overline{b_i^2}$, $\overline{b_i}$ is the neutron scattering length of atom $i$ ($\overline{b_i}=\overline{b_i}^*$, the overbar meaning spin and isotope averaging), $N$ is the number of atoms in the system, $\mathbf{Q}$ is the momentum transfer, $\mathbf{R}_i(t)$ denotes the equilibrium spatial position of atom $i$, $\mathbf{e}^j$ are normalized $3N$-component eigenvectors, $\omega_j$ are eigenfrequencies of the dynamical matrix, $m_i$ is the mass of atom $i$, and $\overline{n_j}$ is the equilibrium occupation number of the vibrational state characterized by the frequency $\omega_j$:

$$\overline{n_j}=\frac{1}{\exp\{\hbar\omega_j/k_BT\}-1}. \tag{3}$$

For isotropic systems, analytical averaging over all $\mathbf{Q}$ directions gives

$$S(Q)=\langle S(\mathbf{Q})\rangle_{\mathbf{\Omega}}=1+\frac{1}{N\langle\overline{b^2}\rangle}\sum_{i\neq i'}\overline{b_i b_{i'}}e^{-W_{ii'}}\times\frac{\sin Q|\mathbf{R}_i-\mathbf{R}_{i'}|}{Q|\mathbf{R}_i-\mathbf{R}_{i'}|}. \tag{4}$$

However, for the finite-sized models under consideration, only a restricted set of $\mathbf{Q}$ vectors is available, i.e., $\mathbf{Q}=\{2\pi n_x/L_x,2\pi n_y/L_y,2\pi n_z/L_z\}$, where $L_\alpha$ are box side lengths and $n_\alpha$ are integer numbers. Averaging over $\mathbf{Q}$ gives

$$S(Q)=\frac{1}{N_Q}\sum_{\mathbf{Q}}S(\mathbf{Q}). \tag{5}$$

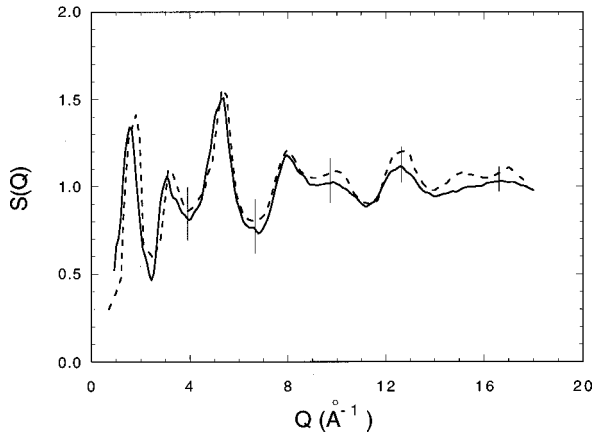


FIG. 3. Dependence of the static structure factor on magnitude of momentum transfer for vitreous silica: The bars are related to numerical averaging over available **Q** only; dashed line, analytical averaging over **Q** directions; solid line, experimental data (Ref. 2).

Here the sum is taken over all available **Q** or $Q$ belonging to a particular range, and $N_Q$ stands for the number of terms in the sum. Results for $S(Q)$ calculated using Eq. (4) for the van Beest–potential–based model are indicated by the solid curve in Fig. 3; the bars indicate the region where the dots lie representing the results of simple (arithmetic) averaging, according to relation (5), over all available **Q** vectors with fixed magnitude of $Q$. The dashed curve is the experimental data.[2] As shown in Fig. 3, the static structure factor of the model fits the experimental curve reasonably well. A slight deviation appears, however, at $Q \gtrsim 15$ Å$^{-1}$. The static structure factor for the Tsuneyuki system shows very similar behavior. However, it is not too difficult to obtain good agreement between calculated and experimental static structural data, and this is characteristic of the majority of reliable structural models of vitreous silica.[22,24,33,34,36]

The analysis presented above shows that the use of the van Beest and Tsuneyuki potentials results in good-quality structural models of vitreous silica. Indeed, both radial and angle distribution functions and the static structure factor are in reasonable agreement with experimental data and the results of *ab initio* MD simulation.[36]

## IV. DYNAMICAL PROPERTIES

Even at zero temperature, atoms vibrate around their equilibrium positions. The amplitude of these vibrations increases with an increase in temperature, but the harmonic approximation is applicable even for sufficiently high temperatures $T \lesssim T_g$. In the harmonic approximation, any atomic vibration can be represented as a linear combination of the normal modes, or eigenvectors, $\{\mathbf{e}^j\}$ $(j=1,\ldots,3N)$, of the dynamical matrix. Here $\{\mathbf{e}^j\}$ is a $3N$-component vector $\{\mathbf{e}_i^j; i=1,\ldots,N\}$ with $\mathbf{e}_i^j$ the real-space vector proportional to the displacement $\mathbf{u}_i^j$ of atom $i$, where $\mathbf{u}_i^j \sim \mathbf{e}_i^j/\sqrt{m_i}$, with $m_i$ being the mass of the $i$th atom. The eigenvectors satisfy the orthonormality and closure conditions

$$\sum_i \mathbf{e}_i^j \mathbf{e}_i^{j'} = \delta_{jj'}, \tag{6}$$

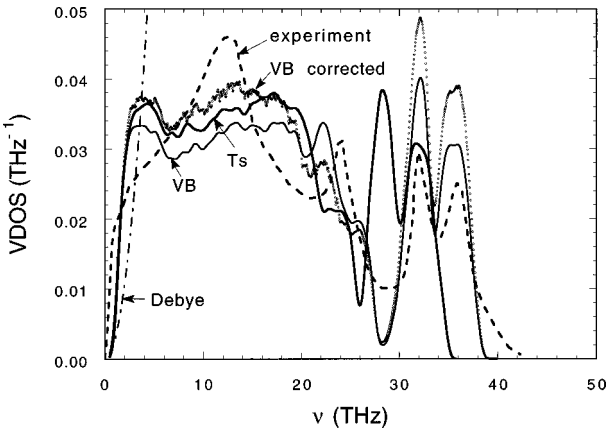


FIG. 4. The vibrational density of states for the van Beest (VB) model (the solid line), the Tsuneyuki (Ts) model (the dashed line), the Debye law (the dot-dashed line), and the experimental data for $v$-$SiO_2$ (the dashed line).

$$\sum_j \mathbf{e}_{\alpha i}^j \mathbf{e}_{\beta i'}^j = \delta_{\alpha\beta}\delta_{ii'}, \tag{7}$$

with $\alpha$ and $\beta$ related to the Cartesian components.[47] In a real-space representation, the Hermitian dynamical matrix is real and symmetric, resulting in $(\mathbf{e}_i^j)^* = \mathbf{e}_i^j$.

### A. Vibrational density of states

One of the most important quantities describing atomic dynamics is the VDOS, defined as

$$g(\omega) = \frac{1}{3N}\sum_{j=1}^{3N} \delta(\omega - \omega_j), \tag{8}$$

where $\omega_j$ are eigenvalues of the dynamical matrix. The function $g(\omega)$ in the whole frequency region is reported in Fig. 4 for the van Beest–potential–based model (the black solid line) and for the Tsuneyuki-potential-based model (the gray solid line), where $\delta$ functions in Eq. (8) have been broadened by Gaussian functions with a typical width $\delta\nu \sim 0.5$ THz which is much larger than the value $(\nu_{\max} - \nu_{\min})/3N \simeq 0.02$ THz for the average separation between eigenvalues for our finite-size model. Here $\nu_{\min} \simeq 1$ THz and $\nu_{\max} \simeq 40$ THz stand for the minimum and maximum frequencies of the vibrational spectrum of the vitreous silica model in question.

Two bands are clearly seen in the spectrum. The highest optical band has two pronounced peaks related to the stretching longitudinal and transverse vibrations of $SiO_4$ units (see below). The structure of the lowest band is more complicated because of the overlap between acoustic and optical bands. Structural disorder in glasses causes a broadening of the sharp band edges of crystals, transforming them into band tails. These band tails have the same origin—structural disorder—as the well-known band tails in the electronic structure of amorphous semiconductors.[48] One of the significant points is that the lowest band tail lies in the background of the acoustic band, and, strictly speaking, the states in this tail are not truly localized, but rather quasilocalized, similar to resonant electron states (e.g., in mixed-valence systems.[49])

The main features of the VDOS shown in Fig. 4 (a wide lower frequency band between 0 and ~25 THz and a narrow

upper band around ~30–40 THz separated by a gap ~1 THz) are similar to those obtained for different structural models of silica[24,30,33,37] and the quartz and cristobalite polymorphs of silica,[16,17,25,29] constructed with various reliable interatomic potentials, including the van Beest potential.[33] However, the VDOS obtained in our simulations using the van Beest potential (the black solid line in Fig. 4) fits the experimental curve[50](the dashed line in Fig. 4) better than does the model constructed using the Tsuneyuki potential[27] (gray solid line in Fig. 4). A deficiency of the Tsuneyuki potential results in a shift of the spectrum in the high-frequency region to lower frequencies by ~5 THz with respect to the experimental VDOS. The vibrational spectrum of vitreous silica, constructed with the aid of a phenomenological three-body interatomic potential,[24] is not free of drawbacks either (the highest-frequency band has no pronounced double-peak structure). Neither the van Beest or Tsuneuki potential can reproduce a pronounced peak in the intermediate-frequency region at 12.5 THz found in the inelastic neutron scattering. This may be due to a deficiency of the potentials which describe the bending modes of $SiO_4^{4-}$ structural units (these modes, as shown below, contribute significantly to the VDOS in the intermediate-frequency range) rather worse than the stretching ones (this drawback is also present at the level of the original *ab initio* calculations[32]). Unfortunately, the majority of phenomenological and semiphenomenological potentials that we know demonstrate this deficiency. The exception is the Feuston-Garofalini potential which results in a peak around 10 THz but does not reproduce the structure of the high-frequency band.[40] However, the rather simple random network[11] or the Bethe lattice[19] and *ab initio* MD-constructed model[37] are free of these drawbacks.

What should be noted when comparing with experimental data is that only the effective VDOS, $g_{\rm eff}(\omega)$, can be measured experimentally using inelastic neutron scattering.[51] In multicomponent atomic systems, $g_{\rm eff}(\omega)$ is connected to the true VDOS, $g(\omega)$, via a correction function $c(\omega)$, given by[34]

$$c(\omega_j)\simeq 1+\frac{A}{3}\sum_\alpha \frac{\overline{b_\alpha^2}}{m_\alpha}[\rho_\alpha(\omega_j)-\rho_\alpha(0)]. \qquad (9)$$

This correction function is derived in Ref. 34 and depends on the relative partial VDOS, $\rho_\alpha(\omega_j)$, related to the partial VDOS, $g_\alpha(\omega_j)$, by

$$\rho_\alpha(\omega_j)=g_\alpha(\omega_j)/g(\omega_j)=\sum_j \sum_{i\ni\alpha} |\mathbf{e}_i^j|^2, \qquad (10)$$

where $i$ signifies all atoms of type $\alpha$ and $j$ denotes a definite eigenmode. This correction function was taken into account in plotting the corrected VDOS $[=c(\omega)g(\omega)]$ in Fig. 4 shown by the circles which is to be compared with the experimental data (the dashed line).

The partial VDOS curves $g_\alpha(\omega)(\alpha=\mathrm{Si,O})$ in Fig. 5 show the relative contribution of atoms of Si (the dashed line in Fig. 5) and O (the dotted line in Fig. 5) to modes at different frequencies. As seen in Fig. 5, oxygen atoms contribute dominantly to the highest optical band and mainly to the lower-frequency band except the region around 22 THz where the motion of silicon atoms is dominant.

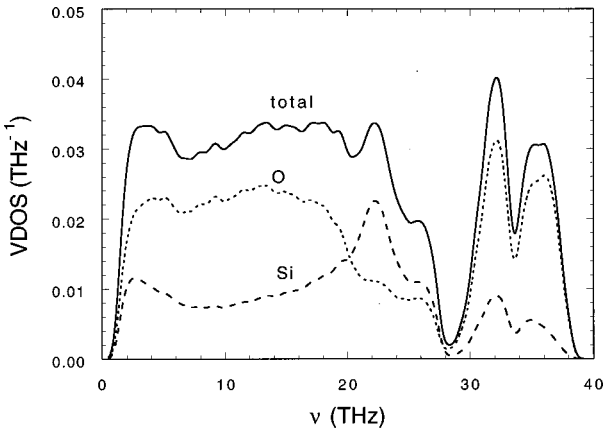


FIG. 5. The relative partial VDOS for Si (the dashed line) and O (the dotted line) atoms compared to the total VDOS (the solid line).

The most frequently used approximation for the VDOS of different substances is the Debye law,[47] $g_{\rm D}(\omega)=3\omega^2/\omega_{\rm D}^3$, with $\omega_{\rm D}=2\pi(9\rho_{\rm at}/4\pi)^{1/3}(c_t^{-3}+2c_l^{-3})^{-1/3}$ being the Debye frequency ($\nu_{\rm D}=\omega_{\rm D}/2\pi\simeq 10.34$ THz or $\hbar\omega_{\rm D}/k_{\rm B}\simeq 497$ K for vitreous silica), where $\rho_{\rm at}=N/V$ is the atomic concentration ($\rho_{\rm at}=0.066$ Å$^{-3}$ in vitreous silica), and $c_t$ and $c_l$ are the transverse and longitudinal velocities of sound, respectively ($c_t=3.75\times10^5$ cm/s and $c_l=5.9\times10^5$ cm/s in vitreous silica.[52,53]) The Debye VDOS for vitreous silica, calculated using experimental values of parameters, is shown by the dot-dashed line in Fig. 4. It is clearly seen that both the computed and experimental VDOS in the low-frequency region ($\omega<5$ THz) appreciably exceed the Debye VDOS. The excess vibrational states in this frequency region form the well-known boson peak.[54] The BP, $g_{\rm BP}(\omega)=g(\omega)-g_{\rm D}(\omega)$, is shown in Fig. 6(a) for the van Beest system. The normalized BP, $\tilde{g}_{\rm BP}(\omega)=[g(\omega)-g_{\rm D}(\omega)]/g(\omega)$, measured in inelastic neutron scattering experiments, is given in Fig. 6(b) for both van Beest (the solid line) and Tsuneyuki (the dashed line) systems. The position of the normalized BP differs from that of $g_{\rm BP}(\omega)$, as clearly seen from Figs. 6(a) and 6(b). The location of the normalized BP in our structural models is around 1.5 THz, which is slightly higher than the experimentally found value 1 THz (see experimental data by Buchenau in Ref. 33). This is a consequence of the finite size of our models resulting in a decrease of the VDOS at $\nu\lesssim\nu_{t,\min}$, with $\nu_{t,\min}=c_t/L\simeq 1.7$ THz being the minimum frequency of the transverse sound wave allowed in a box of finite size $L$. A detailed analysis[55] shows that the vibrational states in the BP region (more precisely, at least in its right wing) are comprised of a set of transverse acoustic waves (in accordance with the results of Ref. 25) characterized by different magnitudes of the wave vector $k$, and forming an acoustic peak around $k_{\max}^j=2\pi\nu^j/c_t$ ($j$ refers to a particular eigenmode) with the half-width $\delta k\sim k$ (i.e., satisfying the Ioffe-Regel criterion). The lowest-frequency eigenmodes are found to have a localized component admixed with the wave component and to exhibit, therefore, quasilocalized behavior.

Excess modes in the BP region influence the temperature dependence of the heat capacity $C_v(T)$ in the temperature range $T\simeq 10$–$30$ K. The vibrational contribution to the heat capacity is given by

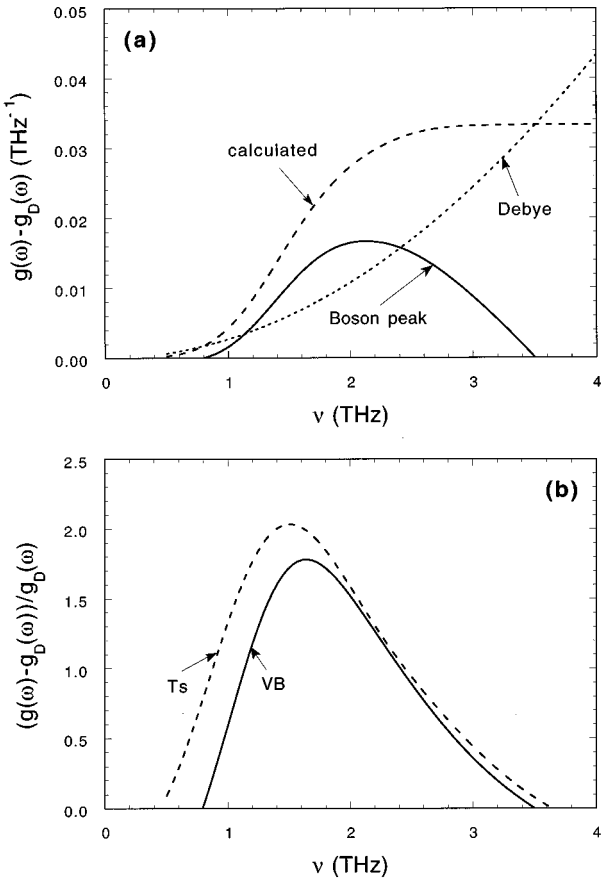


FIG. 6. (a) The boson peak $g(\omega)-g_{\mathrm{D}}(\omega)$ (the solid line), the VDOS for the van Beest model (the dashed line), and the Debye VDOS (the dotted line). (b) The normalized boson peak $[g(\omega)-g_{\mathrm{D}}(\omega)]/g_{\mathrm{D}}(\omega)$ for the van Beest (the solid line) and the Tsuneyuki (the dashed line) models.

$$C_v(T)=\sum_j \left(\frac{\hbar\omega_j}{T}\right)^2 \frac{\exp\{\hbar\omega_j/k_{\mathrm{B}}T\}}{(\exp\{\hbar\omega_j/k_{\mathrm{B}}T\}-1)^2}. \qquad (11)$$

The dependence of $C_v(T)/T^3$ vs $T$ calculated from the model is shown in Fig. 7 (the solid line), compared with

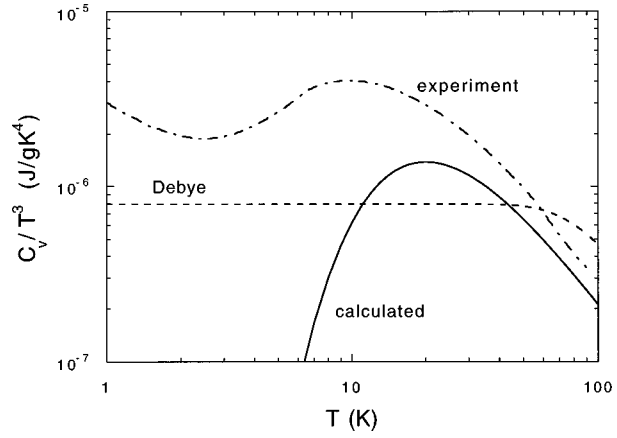


FIG. 7. The dependence of the reduced heat capacity $C_v/T^3$ vs temperature for the van Beest model (the solid line), in the Debye approximation (the dashed line) and the experimental data (the dot-dashed line) (Ref. 7).

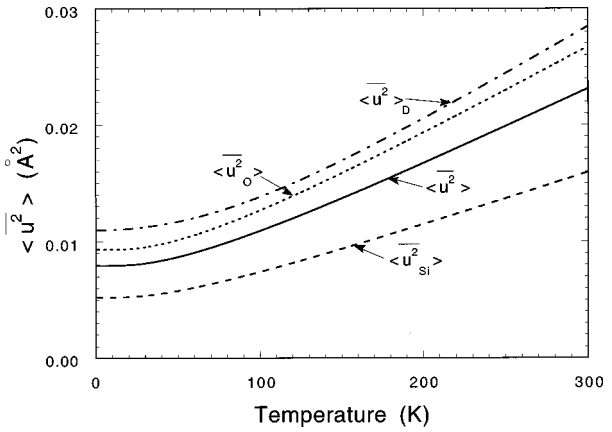


FIG. 8. The mean-square displacement vs temperature for silicon atoms (the dashed line) and for oxygen atoms (the dotted line) for the van Beest model and the quantity averaged over atomic species $\langle\overline{u^2}\rangle$ (the solid line) for the van Beest model compared with $\langle\overline{u^2}\rangle_{\mathrm{D}}$ [see Eq. (15)] in the Debye approximation (the dot-dashed line).

experiment (the dot-dashed line) and the Debye (the dashed line) law. The poor comparison with the experimental data especially at low temperatures $T\lesssim 10$ K is probably due to a deficiency of the finite-size model not describing long-wavelength vibrations which are very important at low temperatures. The existence of the pronounced hump around 10 K is often associated with additional vibrational modes in the low-frequency range. The nature of these modes (the boson peak) is not established yet. However, there are several hypotheses associating these modes with harmonic soft vibrational modes,[56] anharmonic soft modes,[57] soft optic modes,[58] damped acoustic modes,[59] and a crossover from acoustic modes to fractons.[60] In our view, these modes are the states from the bottom part of the lowest optic band strongly hybridized with the acoustic waves (a detailed discussion of this problem will be given elsewhere[55]).

### B. Squared average atomic displacements

Another important characteristic of atomic vibrations is the average atomic displacement $\langle\overline{u_i^2}\rangle$, defined as[47]

$$\langle\overline{u_i^2}\rangle=\frac{\hbar}{m_\alpha}\sum_j \frac{|\mathbf{e}_i^j|^2}{\omega_j}\left(\overline{n}_j+\frac{1}{2}\right), \qquad (12)$$

where the index $i$ refers to atom $i$ in the system. Averaging over all atoms of type $\alpha$ in Eq. (12) results in

$$\langle\overline{u_\alpha^2}\rangle=\frac{\hbar}{N_\alpha m_\alpha}\sum_j \frac{1}{\omega_j}\sum_{i\in\alpha}|\mathbf{e}_i^j|^2\left(\overline{n}_j+\frac{1}{2}\right). \qquad (13)$$

We can rewrite relation (13) using the partial VDOS:

$$\langle\overline{u_\alpha^2}\rangle=\frac{3\hbar}{2n_\alpha m_\alpha}\int g_\alpha(\omega)\frac{2\overline{n}(\omega)+1}{\omega}d\omega, \qquad (14)$$

where $n_\alpha=N_\alpha/N$ stands for the relative number concentration of atoms of type $\alpha$. Plots of $\langle\overline{u_\alpha^2}\rangle$ vs $T$ for oxygen and silicon atoms are reported in Fig. 8. In the high-temperature

regime ($k_B T > \hbar\omega_D$), $\langle \overline{u_\alpha^2} \rangle \sim T$ in accordance with classical statistics $\overline{n(\omega)} \sim T/\hbar\omega$, while at low temperatures $\langle \overline{u_\alpha^2} \rangle$ is temperature independent.

The mean-square displacement $\langle \overline{u^2} \rangle$ averaged over atoms of all species, $\langle \overline{u^2} \rangle = \Sigma_\alpha c_\alpha \langle \overline{u_\alpha^2} \rangle$, can also be calculated in the Debye approximation:[47]

$$\langle \overline{u^2} \rangle_D = \frac{9\hbar}{\omega_D \Sigma_\alpha c_\alpha m_\alpha} \left[ \frac{1}{4} + \left( \frac{k_B T}{\hbar\omega_D} \right)^2 \int_0^{\hbar\omega_D/k_B T} \frac{x\,dx}{e^x - 1} \right]. \tag{15}$$

A comparison of $\langle \overline{u^2} \rangle$ calculated for the van Beest–potential–based model (the solid line) and $\langle \overline{u^2} \rangle_D$ (the dot-dashed line) is given in Fig. 8. The dependence of the mean-squared displacement on temperature in the Debye approximation shows a behavior similar to that following from Eq. (14) but greater in magnitude.

The mean-squared displacement in the Debye-Waller factor is important in describing x-ray and neutron scattering by solids. The value of $\langle \overline{u^2} \rangle$ can be extracted from neutron scattering experiments by comparing the elastic line in neutron scattering with neutron diffraction data.[50,51] The experimental mean-squared displacements at $T = 50$ K are estimated to be $\langle \overline{u_{Si}^2} \rangle = 0.0073$ Å$^2$, $\langle \overline{u_O^2} \rangle = 0.015$ Å$^2$, and $\langle \overline{u^2} \rangle = 0.013$ Å$^2$,[50] and $\langle \overline{u^2} \rangle = 0.0073$ Å$^2$ (Ref. 51) at $T = 33$ K, which agree rather well with our results $\langle \overline{u_{Si}^2} \rangle = 0.0058$ Å$^2$, $\langle \overline{u_O^2} \rangle = 0.01$ Å$^2$, and $\langle \overline{u^2} \rangle = 0.009$ Å$^2$ at $T = 50$ K and $\langle \overline{u^2} \rangle = 0.008$ Å$^2$ at $T = 33$ K. The mean-squared displacements of atoms of different species obtained in Ref. 50 have been calculated by assuming $\langle \overline{u_{Si}^2} \rangle / \langle \overline{u_O^2} \rangle \simeq 0.48$, which is the average value for the various crystalline polymorphs of silica. In our calculations we found $\langle \overline{u_{Si}^2} \rangle / \langle \overline{u_O^2} \rangle$ to increase slightly from 0.56 to 0.59 with increasing temperature from 0 to 300 K. The discrepancy between the calculated values of $\langle \overline{u^2} \rangle$ and experiment is probably due to the absence of very-low-frequency vibrational modes ($\nu \lesssim 1$ THz) caused by the finite size of the model.

### C. Dynamical structure factor

Inelastic neutron scattering is a powerful technique for investigating atomic dynamics, allowing such characteristics as the VDOS for all materials and dispersion curves for crystals to be obtained.[46,61] The dynamical structure factor $S(\mathbf{Q},\omega)$ is proportional to the double-differential cross section for neutrons and can be measured experimentally and compared to theoretical and/or simulation results. For vitreous silica, $S(\mathbf{Q},\omega)$ has been measured in a sufficiently wide region of $Q$-$\omega$ space.[50] A comparison of the results of our simulation of $S(\mathbf{Q},\omega)$ for the van Beest–potential–based model with experimental data[50] is given in Fig. 9 for two frequencies $\nu_1 = 3.02$ THz and $\nu_2 = 11.49$ THz for which experimental data are available (see also Ref. 34 for more detail). The same scaling factor was used when plotting the averaged $S(Q,\omega)$ for both frequencies. This means that the theoretical and experimental curves agree not only in shape, but also quantitatively. The error bars in Fig. 9 refer to numerical averaging of $S(\mathbf{Q},\omega)$ over $\mathbf{Q}$-vector directions similar to that in Eq. (5), while the solid line represents analytical solid-angle averaging, as in Eq. (4). For $\nu_2 = 11.49$ THz, the agreement between experimental data and the results of the simulations is not as good as for $\nu_1 = 3.02$ THz. This is, probably, related to the same failure of the van Beest potential in reproducing a peak in the VDOS around 10 THz.

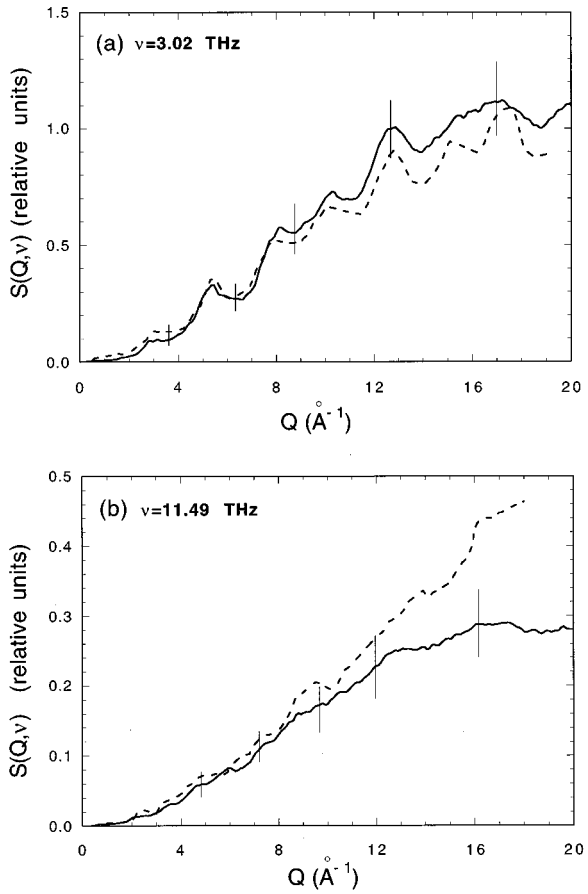


FIG. 9. The dependence of the dynamical structure factor on Q for vitreous silica at two different frequencies for which a comparison with experiment (Ref. 2) is available: (a) $\nu_1 = 3.02$ THz and (b) $\nu_1 = 11.49$ THz (the same notation as in Fig. 3).

The reasonable agreement of our results with experimental data, demonstrated in Fig. 9, supports our choice of interatomic potential used for constructing the structural model of vitreous silica. The use of the Tsuneyuki interatomic potential results in a poor agreement with experimental curves for the $Q$ dependence of the dynamical structure factor at fixed frequencies.

## V. MODE ANALYSIS

A complete knowledge of the eigenvectors and eigenvalues of the dynamical matrix allows us to perform a detailed mode analysis of the system in question. The mode analysis includes the following points: (i) investigation of the degree of mode localization, i.e., the number of atoms involved in a particular mode, (ii) determination of the mode character (acousticlike or opticlike), (iii) assignment of definite structural-unit vibrations to a particular mode, and (iv) ascertaining the origin of eigenmodes in different frequency ranges.

### A. Mode localization

In a perfect crystal, all vibrational modes extend over the whole system. This is a consequence of long-range order. Structural disorder results in the appearance of localized modes. Localization can be quantitatively described using the participation ratio, $p_j$, for the eigenmode $j$,[11]

$$p_j = \left( \sum_{i=1}^{N} |\mathbf{u}_i^j|^2 \right)^2 \cdot \left( N \sum_{i=1}^{N} |\mathbf{u}_i^j|^4 \right)^{-1}. \tag{16}$$

The participation ratio is $p \sim 1$ for an extended mode ($p=1$ for the rigid-body displacement at which all atoms are equally displaced) and, in particular, $p \simeq 0.6$ for a plane wave, while $p \sim 1/N$ for a mode strongly localized to a few atomic sites. Henceforth, the displacement eigenvectors $\mathbf{u}^j$ are normalized to unity, i.e., $\Sigma_{i=1}^{N} |\mathbf{u}_i^j|^2 = 1$.

The frequency dependence of the participation ratio for the van Beest–potential model of vitreous silica is shown in Fig. 10(a). As seen from Fig. 10(a), states in the middle of the lower band are extended and characterized by values of the participation ratio close to 0.5. States belonging to a narrow high-frequency band in the region between 30 and 40 THz are characterized by smaller values of the participation ratio ($p \sim 0.2$) in the middle of the band and very low values of the participation ratio ($p \sim 10^{-2}$) in the band tails. This is due to a higher degree of localization of states in this band which are comprised of just a few symmetric and asymmetric vibrational modes of $SiO_4$ tetrahedra (see below). A detailed analysis of mode localization will be given elsewhere.

Structural disorder leads to a broadening of band edges and the appearance of band tails containing localized modes. These tails are clearly seen (small values of the participation ratio) at the top of the lower band and on both sides of the higher band. The appearance of the band tails results in a narrowing of the band gap to $\Delta\nu_g \simeq 1$ THz in vitreous silica (cf. $\Delta\nu_g \simeq 1$–5 THz in $\alpha$-cristobalite[25,16] and $\Delta\nu_g \simeq 3$ THz in $\alpha$-quartz[17]). A similar narrowing of the gap has also been found in $\beta$-cristobalite[28] due to dynamical disorder.

These changes in the band structure are also characteristic of electronic excitations in disordered materials.[48] A particular feature of atomic vibrations in some disordered structures is, we propose,[55] that long-wavelength acoustic excitations coexist with the lowest optic band states; i.e., the acoustic band overlaps the lowest optic band. This effect gives rise to a strong hybridization between acoustic waves and optic band states. Therefore the lowest optic-band-tail states (which would be localized in the absence of mixing) are actually quasilocalized because of this hybridization and hence resemble electronic in-band resonances. The participation ratios of these states are one order of magnitude higher than those of the truly localized tail states at higher frequencies. The lowest value of the participation ratio for the lowest frequencies has been found for the Tsuneyuki potential based model ($p_{\min} \simeq 0.06$). These quasilocalized states are actually a mixture of an extended wave-like constituent and a localized one (see Ref. 55 for more details).

In order to investigate the contribution of different atomic species to the participation ratio, we calculated the partial participation ratios for silicon, $p_{\mathrm{Si}}$, and oxygen, $p_{\mathrm{O}}$, atoms [see Figs. 10(b) and 10(c)]. Values of $p_{\mathrm{Si}}$ and $p_{\mathrm{O}}$ were found from Eq. (16) with the summation made only over silicon or oxygen atoms. As seen in Figs. 10(b) and 10(c), the dependence $p_{\mathrm{O}}(\nu)$ mainly coincides with the frequency dependence of the total participation ratio, meaning that oxygen atoms define the localization behavior of the eigenmodes.

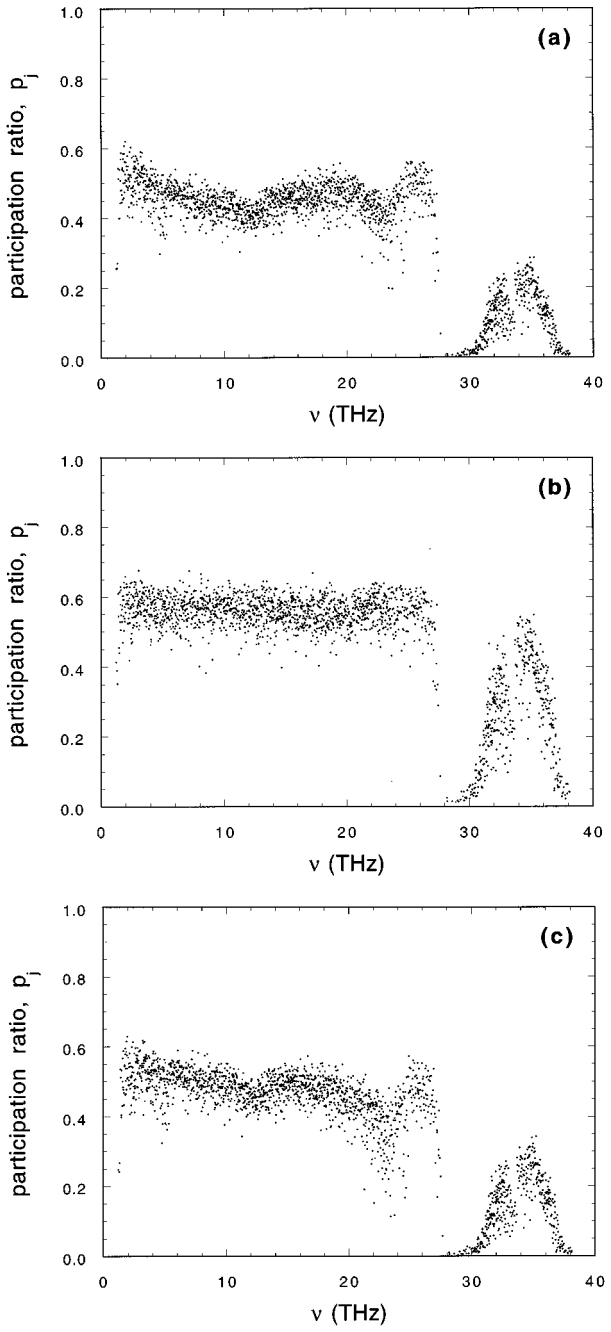


FIG. 10. The dependence of the participation ratio on frequency: (a) total and partial [for (b) silicon and (c) oxygen].

### B. Phase quotient

Atomic vibrations in crystals (i.e., phonons) can be divided into acoustic and optic modes. In acoustic phonons, neighboring atoms move practically in phase, while in optic modes, the relative motion is mainly out of phase. In disordered structures, atomic vibrations cannot be characterized by a definite wave vector (see also Ref. 55), and a division of

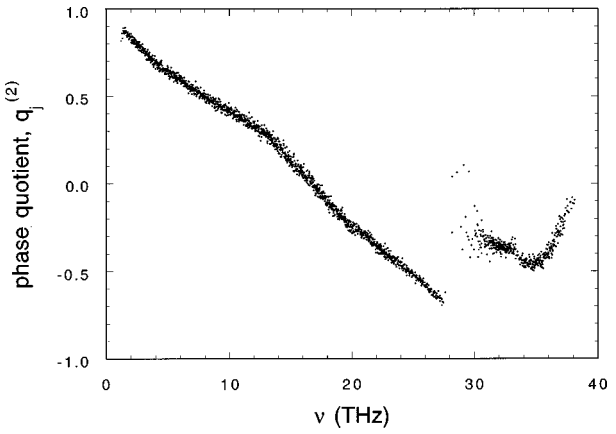


FIG. 11. The variation of weighted phase quotient with frequency.

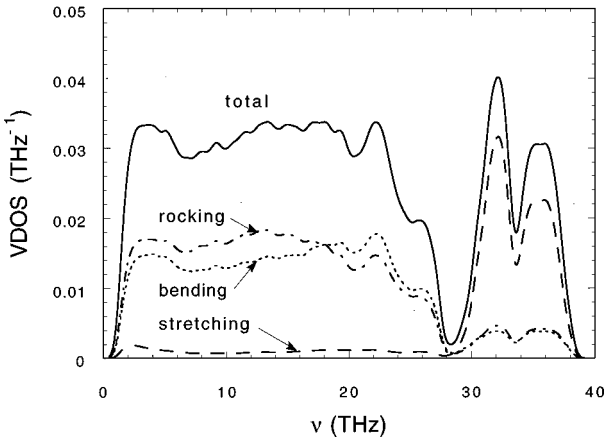


FIG. 12. The stretching (dashed), bending (dotted), and rocking (dot-dashed) components of the total VDOS (solid).

atomic vibrations into acoustic and optic modes is not possible in general. However, some phase characteristics can be calculated for vibrational modes in disordered structures. One such quantity is the phase quotient for mode $j$:[11,24]

$$q_j=\langle\cos\theta\rangle_j=\frac{1}{N_b}\sum_i\sum_{i'}\frac{\mathbf{u}_i^j\cdot\mathbf{u}_{i'}^j}{|\mathbf{u}_i^j|\cdot|\mathbf{u}_{i'}^j|},\tag{17}$$

which is just the average cosine of the angle between displacement vectors of neighboring atoms. In Eq. (17), $i$ runs over all silicon atoms while $i'$ numerates all the nearest oxygen neighbors of silicon atoms, $N_b$ being the number of valence bonds. In terms of values of the phase quotient, it is possible to speak about acousticlike and opticlike modes in disordered structures. In acousticlike waves, all atoms move practically in phase, and the phase quotient is close to unity. In optic modes, the relative motion of atoms is out of phase, and $q_j\simeq-1$. For delocalized modes, different atoms give similar contributions to $q_j$ in averaging Eq. (17). For localized modes, this is not the case, and in order to take into account the different contributions of various atoms to the phase quotient we defined the weighted phase quotient, $q_j^{(n)}$, weighted by the $n$th power of the amplitude of the eigenvector, which for $n=2$ is

$$q_j^{(2)}=\frac{1}{\sum_{i,i'}|\mathbf{e}_i^j|^2}\sum_i\sum_{i'}\frac{\mathbf{u}_i^j\cdot\mathbf{u}_{i'}^j}{|\mathbf{u}_i^j|\cdot|\mathbf{u}_{i'}^j|}\cdot|\mathbf{e}_i^j|^2.\tag{18}$$

The dependence of the weighted phase quotient on frequency is given in Fig. 11. The weighted phase quotient tends to unity with decreasing frequency, indicating an increasing acousticlike character of the eigenmodes. A slight decrease of $q_j^{(2)}$ at the lowest frequencies reflects their quasilocalized nature. In order to investigate this point in more detail, we extracted the localized constituent of the lowest-frequency eigenmode and found its phase quotient to be $\lesssim0.5$, indicating a more opticlike character of the localized component (a detailed analysis will be presented elsewhere; see also Ref. 55). At high frequencies, the weighted phase quotient is mainly negative, meaning that eigenmodes in this frequency range can be regarded as opticlike vibrations. An abrupt change in the weighted phase quotient around the band gap (at $\nu\simeq27$ THz) indicates a different nature of the opticlike vibrations in the bands separated by the gap.

### C. Stretching, bending, and rocking

The structure of vitreous silica consists of corner-shared tetrahedral $SiO_4$ units. These units are connected to each other via bridging oxygen atoms. Twofold-coordinated bridging oxygen atoms can move quite easily compared to fourfold-coordinated silicon atoms and have been supposed to give the main contribution to the atomic vibrations in this system.[6,11,19] The simplest and most frequently used procedure for describing oxygen motion is to decompose its displacement into three components along three orthogonal directions, $\mathbf{u}_i^j=\mathbf{u}_{is}^j+\mathbf{u}_{ib}^j+\mathbf{u}_{ir}^j$, related to bond-stretching ($\mathbf{u}_{is}^j$), bond-bending ($\mathbf{u}_{ib}^j$), and rocking ($\mathbf{u}_{ir}^j$) motions.[11] Then the squared average displacement along these directions can be calculated according to the following expression:

$$|r^j|_{s,b,r}^2=\frac{1}{\sum_i|\tilde{\mathbf{u}}_i^j|^2}\sum_i|\tilde{\mathbf{u}}_i^j|_{s,b,r}^2,\tag{19}$$

Bearing in mind that the two silicon atoms $i'$ that are neighbors of the oxygen atom $i$ move as well, only the relative motion of the oxygen atom has been decomposed into stretching, bending, and rocking components in Eq. (19), so that $\tilde{\mathbf{u}}_i^j=\mathbf{u}_i^j-(\mathbf{u}_{\mathrm{Si}1}^j+\mathbf{u}_{\mathrm{Si}2}^j)/2$ is the displacement of oxygen atom $i$ relative to the average displacement of its nearest silicon neighbors. The convolution of $|r^j|_{s,b,r}^2$ with the total VDOS decomposes $g(\omega)$ into the stretching, bending, and rocking components, $g(\omega)=g_s(\omega)+g_b(\omega)+g_r(\omega)$, where

$$g_{s,b,r}(\omega)=\frac{1}{3N}\sum_j|r^j|_{s,b,r}^2\delta(\omega-\omega_j).\tag{20}$$

The frequency dependences of the stretching, bending, and rocking components of VDOS are presented in Fig. 12. It is clearly seen that stretching motion (the dashed line) is important only for the highest opticlike band ($\nu\sim30$–$40$ THz), while bending (the dotted line) and rocking (the dot-dashed) contribute equivalently at lower frequencies. A similar analysis made for a Bethe-lattice model[19] shows that stretch-

ing results in a broad asymmetric peak around 30 THz, which agrees quantitatively with our results. Rocking motion in the Bethe-lattice model causes a peak around 13.5 THz, while bending leads to a broad triangle-shaped peak at 16.5 THz and a narrow peak at 21 THz. The peaks for rocking and bending do not agree with our results.

### D. Projections onto vibrational modes of different structural units

Another way of investigating the atomic motion for different eigenmodes is to project the eigenvectors onto various vibrational modes of typical structural units. The projection $r^j_{\mathbf{A},i}$ of the displacement eigenvector $\mathbf{u}^j$ onto the vibrational displacement vector $\mathbf{A}_{(i)}$ of the structural unit $i$ can be written as a dot product of these vectors:

$$r^j_{\mathbf{A},i}=\sum_{i'(i)} \mathbf{u}^j_{i'}\cdot\mathbf{A}_{i'(i)}, \tag{21}$$

where the sum is taken over all atoms $i'$ comprising the structural unit $i$. The displacement vector $\mathbf{A}_{(i)}$ normalized to unity consists of $3N_{(i)}$ components which are the Cartesian coordinates of the displacement vectors of each of the $N_{(i)}$ atoms comprising the structural unit $i$. The squared value of the projection in Eq. (21) characterizes contributions of the vibrational motion of a definite type of the structural unit $i$ to the eigenmode $j$. Averaging of the squared projections over all structural units of a definite type results in

$$(r^{j(n)}_{\mathbf{A}})^2=\frac{1}{\Sigma_i (w^j_i)^n}\sum_i (w^j_i)^n (r^j_{\mathbf{A},i})^2, \tag{22}$$

with $n=0,1,2,\ldots$ being the exponent of the weight $w^j_i$ given by

$$w^j_i=\left[\sum_{i'(i)} |\mathbf{e}^j_{i'}|^2\right]^{1/2}. \tag{23}$$

For $n\geqslant 1$, the weight $(w^j_i)^n$ takes into account the different contributions of the various structural units $i$ in the total eigenmode $j$. Use of the weighted projections makes sense for localized modes in order to enhance the contribution of the units at which the mode is mainly localized.

The displacement eigenvector $\mathbf{u}^j_{i'}$ can be renormalized only over atoms comprising the structural unit, and the projection $\tilde{r}^j_{\mathbf{A}_{(i)}}$ of this renormalized vector onto vibrational mode $\mathbf{A}_{(i)}$, viz.,

$$\tilde{r}^j_{\mathbf{A}_{(i)}}=r^j_{\mathbf{A}_{(i)}}\Big/\left[\sum_{i'(i)} |\mathbf{u}^j_{i'}|^2\right]^{1/2}, \tag{24}$$

does not give information about the contribution of the **A** mode to the total eigenvector but characterizes the type of motion of the structural unit $i$; i.e., it shows the relative contribution of the **A** mode to the vibrational motion of the structural unit $i$ in comparison with contributions of other vibrational modes of this unit. The averaging of the squared renormalized projection with weights given by Eq. (23) over all structural units gives rise to the expression

$$(\tilde{r}^{j(n)}_{\mathbf{A}})^2=\frac{1}{\Sigma_i (w^j_i)^n}\sum_i (w^j_i)^n (\tilde{r}^j_{\mathbf{A}_{(i)}})^2, \tag{25}$$

which can be used (with $n=0$) to calculate the partial VDOS $g_{\mathbf{A}}(\omega)$ for different types (**A**) of vibrations of the structural unit,

$$g_{\mathbf{A}}(\omega)=\frac{1}{3N}\sum_j (\tilde{r}^{j(0)}_{\mathbf{A}})^2\delta(\omega-\omega_j). \tag{26}$$

If the vibrational modes of the structural unit comprise a complete set, then

$$g(\omega)=\sum_{\mathbf{A}} g_{\mathbf{A}}(\omega). \tag{27}$$

The weighted squared renormalized projections with $n\geqslant 1$ can be used to characterize localized vibrational modes. It should be noted that the use of weights in Eq. (25) cannot compensate for the renormalization of the displacement eigenvector in Eq. (24).

Vitreous silica can be imagined as being comprised of structural units of different types. The nonlinear three-atom Si-O-Si units and corner-shared tetrahedral $SiO_4$ units are usually considered[11,17,19] to be the basic ones. In the ideal case, these structural units (isolated molecules) have the point-group symmetries $C_{2v}$ and $T_d$, respectively. The most convenient way to characterize the vibrations of these units is to introduce symmetry coordinates for which the dynamical matrix has a block form. These coordinates transform like different irreducible representations (species) of the corresponding point group. In the case of Si-O-Si structural units, one symmetry coordinate (asymmetric stretching) belongs to the nondegenerate species $B_1$ and two other symmetry coordinates (symmetric stretching and bending) belong to the nondegenerate species $A_1$. In the case of $SiO_4$ units, one symmetry coordinate (symmetric stretching) belongs to the nondegenerate species $A_1$, a single pair of symmetry coordinates (bending) belongs to the doubly degenerate species $E$, and two triplets (asymmetric stretching and bending) belong to the triply degenerate species $F_2$.[62] The symmetry coordinates of the species $B_1$ (for Si-O-Si) and of the species $A_1$ and $E$ (for $SiO_4$) coincide with the normal coordinates of these structural units while the others do not and the normal coordinates are the linear combinations of the symmetry coordinates belonging to the same species (e.g., of the $F_2$-stretching and the $F_2$-bending coordinates in case of $SiO_4$). The coefficients in these linear combinations are related to the off-diagonal dynamical matrix elements, the values of which depend on the specific model used to describe the potential field. Therefore the normal modes cannot be used in a projection analysis.

The symmetry coordinates do not describe the motion of the structural unit as a whole unit (solid-body displacements and rotations) but are related to the internal coordinates, i.e., the bond angles and interatomic distances. Bearing this in mind, we define and consider the relative displacement eigenvector $\mathbf{u}^j_{i(i_0)}$,

$$\mathbf{u}^j_{i(i_0)}=(\mathbf{u}^j_i-\mathbf{u}^j_{i_0})/\sqrt{C^j_{i_0}}, \tag{28}$$

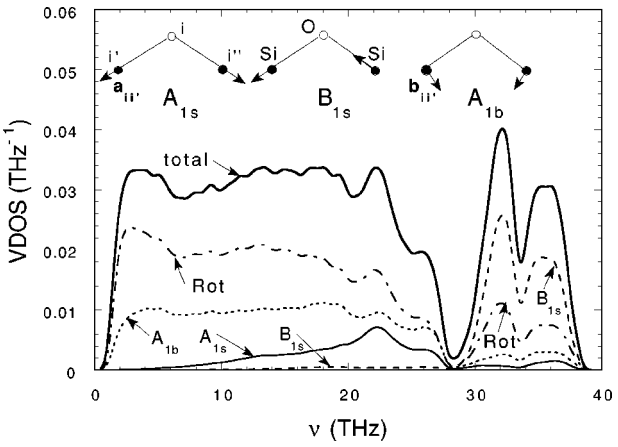


FIG. 13. The partial VDOS for the projections onto the vibrations of Si-O-Si structural units: $A_1$ stretching (the gray solid line, $A_{1s}$), $B_1$ stretching (the dashed line, $B_{1s}$), $A_1$ bending (the dotted line; $A_{1b}$), solid-unit rotations (the dot-dashed line), and their sum (the black solid line) coinciding with the total VDOS. The atomic displacements in Si-O-Si units for symmetric ($A_{1s}$) and asymmetric ($B_{1s}$) stretching and also bending ($A_{1b}$) are shown schematically in the inset.

with $C^j_{i_0}$ the normalization constant given by

$$C^j_{i_0}=\sum_i |\mathbf{u}^j_i-\mathbf{u}^j_{i_0}|^2. \tag{29}$$

Here $i_0$ denotes the central atom in the structural unit (oxygen for Si-O-Si and silicon for $SiO_4$) which thus becomes the reference point for the components of the displacement eigenvector. The symmetry coordinates are defined below in consistency with Eq. (28) so that the central atom is immobile for them as well. To obtain a ''complete'' set of vibrations of the structural unit we also added three solid-unit rotations to the symmetry modes.

#### *1. Projection onto vibrations of Si-O-Si structural units*

Here we present the results of projecting the eigenmodes onto the symmetry vibrational coordinates of Si-O-Si units. Three symmetry displacement vectors characterizing symmetric ($A_1$) and asymmetric ($B_1$) stretching, and also bending ($A_1$), can be defined for these units (see also Ref. 62):

$$\mathbf{S}^{(A_1)}_{(i)}=\frac{1}{\sqrt{2}}\{\hat{\mathbf{a}}_{ii'},\mathbf{0},\hat{\mathbf{a}}_{ii''}\},\quad \mathbf{S}^{(B_1)}_{(i)}=\frac{1}{\sqrt{2}}\{\hat{\mathbf{a}}_{ii'},\mathbf{0},-\hat{\mathbf{a}}_{ii''}\},$$

$$\mathbf{B}^{(A_1)}_{(i)}=\frac{1}{\sqrt{2}}\{\hat{\mathbf{b}}_{i'i''},\mathbf{0},\hat{\mathbf{b}}_{i''i'}\}, \tag{30}$$

with $\hat{\mathbf{a}}_{i'i''}$ being the unit vector directed from atom $i'$ to atom $i''$ and $\hat{\mathbf{b}}_{i'i''}$ the unit vector perpendicular to the bond between atoms $i$ and $i'$ and directed from atom $i'$ to atom $i''$ as shown in the inset in Fig. 13. The first component of the displacement vectors in Eq. (30) characterizes the displacement of atom $i'$, the second of atom $i$ (immobile), and the third of atom $i''$.

For all Si-O-Si structural units, we calculated the projections of the renormalized eigenvectors onto symmetry coordinates of these units according to Eqs. (21)–(25), using the expressions in Eq. (30) for $\mathbf{A}_{(i)}$ and replacing $\mathbf{u}^j_{i'}$ by the relative displacement eigenvector $\mathbf{u}^j_{i'(i)}$ defined in Eq. (28). Then, an averaging over all units has been made as in Eq. (25) with $n=0$ and the partial VDOS for different projections were calculated in accordance with Eq. (26). The results are shown in Fig. 13, where the partial VDOS for the solid unit rotations is also represented by a dot-dashed line. The rotations have been made around three perpendicular axes passing through the central (oxygen) atoms; then the squared projections onto rotations have been summed for every unit and averaged over all units. It follows from Fig. 13 that the symmetric stretching of Si-O-Si units (the gray solid line) is a maximum at frequencies around 22 THz (although this is not the dominant contribution overall) and asymmetric stretching (the dashed line) contributes at frequencies in the region of the two peaks at 32 and 36 THz, while bending (the dotted line) is essential in a broad region between 1 and 27 THz. Rotational motion (the dot-dashed line) contributes to the motion of Si-O-Si units in the whole frequency range: not very appreciably in the higher-frequency band, comparable to bending in the middle of the lower-frequency band and appreciably in the low-frequency region. The latter feature is quite important in clarifying the nature of the low-frequency vibrations. The sum of all partial VDOS (the solid black line) calculated according to Eq. (27) coincides with the total VDOS. The lack of coincidence of these two lines, especially in the lower-frequency band, is due to the fact that the Si-O-Si structural units in our structural model are not perfectly symmetric ($C_{2v}$) three-atom ''molecules'' and the displacement vectors [Eq. (30)] plus three solid-unit rotations do not form an exactly complete set of vectors. Use of the weighted projections [$n=2$ or $n=4$ in Eq. (25)] leads just to small corrections in the partial VDOS.

We have also calculated the projections of nonrenormalized eigenvectors onto the symmetry displacement vectors for Si-O-Si units using Eqs. (21)–(23). Such projections take into account the different amplitudes of a definite eigenvector on the various structural units and therefore give more precise information about the type of atomic motion for a definite eigenmode. Nonweighted ($n=0$) squared projections onto symmetric (solid circles) and asymmetric (open circles) stretching, bending (open diamonds), and rotations (crosses) are shown in Fig. 14(a). It follows from this figure that symmetric and asymmetric stretching within Si-O-Si units takes place mainly for eigenmodes around 22 THz and around 32 and 36 THz, respectively, which agrees with the peak positions of $g_{S^{(A_1)}}(\omega)$ and $g_{S^{(B_1)}}(\omega)$ in Fig. 13. The data for bending, however, show an appreciable maximum near the upper edge of the lower-frequency band (27 THz) which is not seen in Fig. 13. This means that bending motion gives the essential contribution to the eigenmodes mainly in this frequency region. The squared projection onto rotational motion has a pronounced maximum at 22 THz, which is not seen in Fig. 13 as well. In this respect, we would like to stress again that the commonly used partial VDOS (Refs. 19 and 26) for different projections gives information just about how atoms move within the structural units on average, not taking into account the different amplitudes of vibrations in various units.

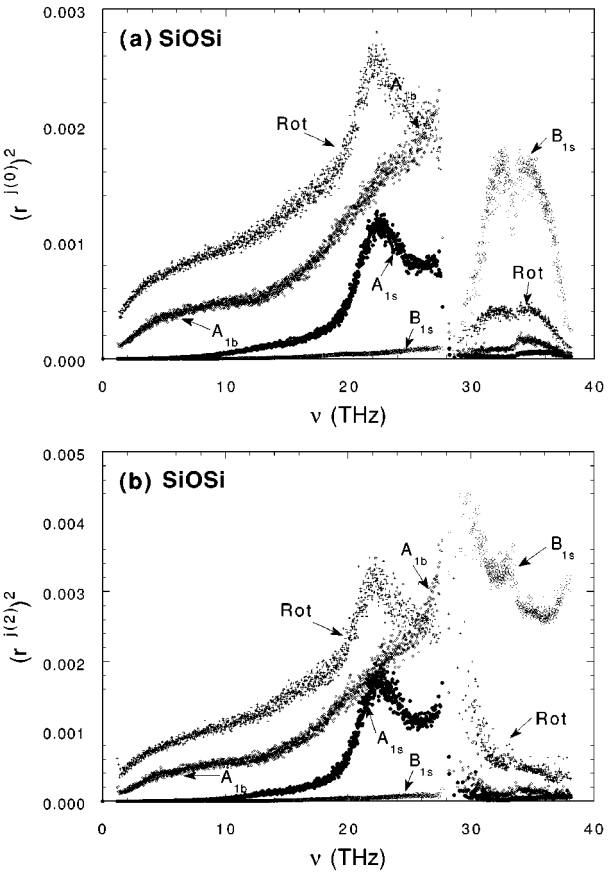


FIG. 14. The squared projections of the eigenvectors onto Si-O-Si symmetry coordinates: $A_1$ stretching (solid circles), $B_1$ stretching (open circles), $A_1$ bending (open diamonds), and onto solid-unit rotations (crosses): (a) nonweighted; (b) weighted with $n=2$.

The use of weighted projections [e.g., $n=2$ in Eq. (22)] enhances the contribution of localized vibrational states and allows conclusions to be made about the type of atomic motion for localized modes. The weighted ($n=2$) squared projections of nonrenormalized eigenvectors onto different symmetry displacement vectors are shown in Fig. 14(b). The difference between Figs. 14(a) and 14(b) occurs mainly in the high-frequency region around the band edges where the eigenmodes are strongly localized. It is seen from Fig. 14(b) that the localized states at the top of the lowest-frequency band ($\sim$28 THz) are characterized by bending motion of Si-O-Si structural units, while the localized states at the bottom of the higher-frequency band ($\sim$29 THz) are dominated by asymmetric stretching and rotational motion. Practically only asymmetric stretching takes place for the states at the top of the higher-frequency band ($\sim$39 THz). We also mention a slight increase in the values of the weighted squared projections onto rotational and bending coordinates for the lowest frequencies ($\sim$1 THz), which can be related to the quasilocalization of these states.

#### *2. Projection onto vibrations of $SiO_4$ tetrahedra*

Similar projectional analyses have been performed for $SiO_4$ structural units, the results of which are presented below. The perfect $SiO_4$ tetrahedron has nine symmetry

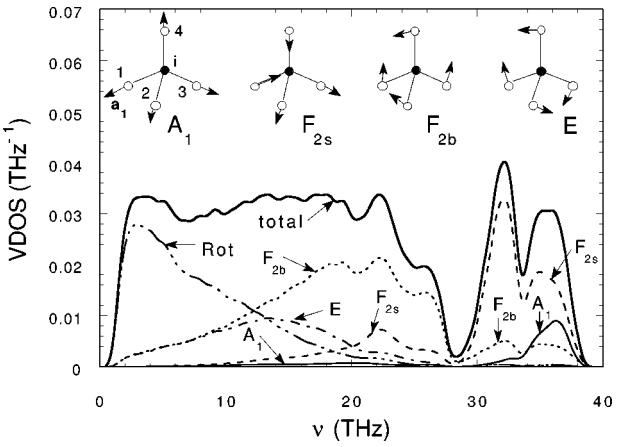


FIG. 15. The partial VDOS for the projections onto the vibrations of $SiO_4$ structural units: $A_1$ stretching (the solid gray line), $F_2$ stretching (the dashed line), $F_2$ bending (the dotted line), $E$ bending (the dot-dashed line), solid-unit rotations (the triple dot-dashed line), and their sum (the black solid line) coinciding with the total VDOS. The atomic displacements in $SiO_4$ units for symmetric ($A_1$) and asymmetric ($F_{2s}$) stretching and also $F_2$ and $E$ bending are shown schematically in the inset.

modes.[62] The symmetric-stretching displacement eigenvector ($A_1$ symmetry) is given by the following relation:

$$\mathbf{S}^{(\mathrm{A}_1)}=\frac{1}{\sqrt{4}}\{\mathbf{0},\hat{\mathbf{a}}_1,\hat{\mathbf{a}}_2,\hat{\mathbf{a}}_3,\hat{\mathbf{a}}_4\}, \tag{31}$$

where the first component characterizes the displacement of the central silicon atom $i$ (the index $i$ is omitted below) and the rest are related to the oxygen atoms $i'=1,\ldots,4$ (the unit vectors $\hat{\mathbf{a}}_{i'}$ are directed from atom $i$ to atoms $i'$; see inset in Fig. 15). The three degenerate asymmetric-stretching coordinates ($F_2$ symmetry) are

$$\mathbf{S}_1^{(F_2)}=\frac{1}{\sqrt{4}}\{\mathbf{0},\hat{\mathbf{a}}_1,\hat{\mathbf{a}}_2,-\hat{\mathbf{a}}_3,-\hat{\mathbf{a}}_4\},$$

$$\mathbf{S}_2^{(F_2)}=\frac{1}{\sqrt{4}}\{\mathbf{0},\hat{\mathbf{a}}_1,-\hat{\mathbf{a}}_2,-\hat{\mathbf{a}}_3,\hat{\mathbf{a}}_4\},$$

$$\mathbf{S}_3^{(F_2)}=\frac{1}{\sqrt{4}}\{\mathbf{0},\hat{\mathbf{a}}_1,-\hat{\mathbf{a}}_2,\hat{\mathbf{a}}_3,-\hat{\mathbf{a}}_4\}. \tag{32}$$

Bending coordinates can be divided into two groups: three degenerate coordinates ($F_2$ symmetry) ,

$$\mathbf{B}_1^{(F_2)}=\frac{1}{\sqrt{4}}\{\mathbf{0},\hat{\mathbf{b}}_{12},\hat{\mathbf{b}}_{21},-\hat{\mathbf{b}}_{34},-\hat{\mathbf{b}}_{43}\}, \tag{33}$$

$$\mathbf{B}_2^{(F_2)}=\frac{1}{\sqrt{4}}\{\mathbf{0},\hat{\mathbf{b}}_{14},-\hat{\mathbf{b}}_{23},-\hat{\mathbf{b}}_{32},\hat{\mathbf{b}}_{41}\},$$

$$\mathbf{B}_3^{(F_2)}=\frac{1}{\sqrt{4}}\{\mathbf{0},\hat{\mathbf{b}}_{13},-\hat{\mathbf{b}}_{24},\hat{\mathbf{b}}_{31},-\hat{\mathbf{b}}_{42}\}$$

and two degenerate coordinates ($E$ symmetry),

$$\mathbf{B}_1^{(E)} = B_1\{\mathbf{0}, 2\hat{\mathbf{b}}_{12} - \hat{\mathbf{b}}_{13} - \hat{\mathbf{b}}_{14}, 2\hat{\mathbf{b}}_{21} - \hat{\mathbf{b}}_{23} - \hat{\mathbf{b}}_{24}, 2\hat{\mathbf{b}}_{34} - \hat{\mathbf{b}}_{31} - \hat{\mathbf{b}}_{32}, 2\hat{\mathbf{b}}_{43} - \hat{\mathbf{b}}_{41} - \hat{\mathbf{b}}_{42}, \},$$

$$\mathbf{B}_2^{(E)} = B_2\{\mathbf{0}, (\hat{\mathbf{b}}_{13} - \hat{\mathbf{b}}_{14}), -(\hat{\mathbf{b}}_{23} + \hat{\mathbf{b}}_{24}), (\hat{\mathbf{b}}_{31} - \hat{\mathbf{b}}_{32}), -(\hat{\mathbf{b}}_{41} + \hat{\mathbf{b}}_{42})\}, \quad (34)$$

with $\hat{\mathbf{b}}_{i'i''}$ being the unit vector perpendicular to the bond between the central silicon atom and an oxygen atom $i'$ and directed from atom $i'$ to atom $i''$, as shown in the inset in Fig. 15, and $B_{1,2}$ are normalization constants, with $|\mathbf{B}_{1,2}^{(E)}| = 1$.

First, we calculated the projections of the renormalized eigenvectors onto these symmetry displacement vectors [see Eq. (24)] for every tetrahedron and then averaged them over all tetrahedra using Eq. (25) with $n=0$. The convolution of the averaged squared renormalized projections with the total VDOS according to Eq. (26) results in the partial VDOS for different type of symmetry vibrations and solid-unit rotations which are presented in Fig. 15. The symmetric stretching (the gray solid line), as seen from Fig. 15, gives a contribution to the motion of $SiO_4$ units only for states around the upper peak at 37 THz in the high-frequency band, while the asymmetric stretching (the dashed line) contributes appreciably to the motion of $SiO_4$ units for the states in both peaks at 32 and 37 THz. The stretching vibrations of $SiO_4$ tetrahedra give practically no contribution to the motion of the tetrahedra at frequencies below the band gap ($\nu \lesssim 27$ THz) except for an insubstantial contribution of asymmetric stretching to the states in the peak around 22 THz. This picture agrees with the results discussed in Refs. 26, 30 and 37 but contradicts the conclusions of Ref. 18. It should be noted, however, that the authors of Ref. 26 found essentially a larger contribution of $A_1$ stretching for the states in the upper peak 37 THz and an additional contribution of this type of motion for the states in a peak around 21 THz. The $F_2$ stretching found in Ref. 26 gives a contribution to the states in a peak at 24 THz in the lower band (as compared to the peak at 22 THz obtained in our calculations).

The bending vibrations, in contrast to stretching, provide the major contribution to $SiO_4$ motion for the states in the intermediate-frequency region in the vicinity of the broad peaks at 15 THz ($E$ bending shown by the dot-dashed line in Fig. 15) and 20 THz ($F_2$ bending, dotted line). The authors of Ref. 26 generated a structural model of silica based on a different interatomic potential and found sharper peaks at 12 THz ($E$ bending) and at 14.5 THz which are quite different from those obtained in our simulations, the result, probably, of the use of a different interatomic potential.

The rotational motion (the triple-dot-dashed line) gives the main contribution to $SiO_4$ motion for the states in the lowest part of the frequency spectrum. This feature is rather important from our viewpoint to clarify the origin of the low-frequency vibrations. The sum of all partial VDOS for different squared projections, including rotational ones, is represented by the solid black line in Fig. 15 which coincides with the calculated total VDOS. The partial VDOS calculated with the use of weighted projections differ only slightly from those presented in Fig. 15.

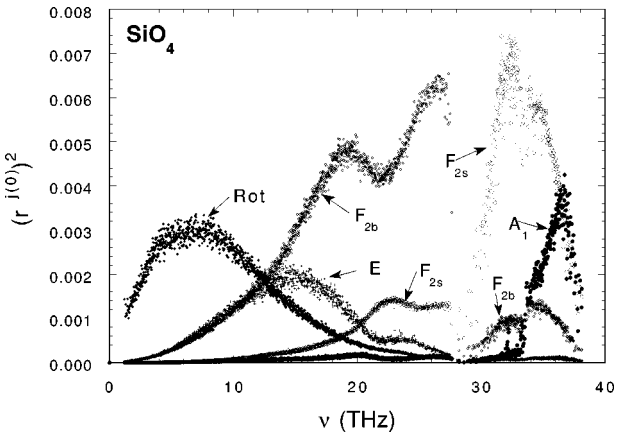


FIG. 16. The squared nonweighted projections of the eigenvectors onto $SiO_4$ symmetry coordinates: $A_1$ stretching (solid circles), $F_2$ stretching (open circles), $F_2$ bending (open diamonds), $E$ bending (solid diamonds) and onto solid-unit rotations (crosses).

The projections of nonrenormalized eigenvectors onto symmetry displacement vectors for $SiO_4$ units [see Eqs. (21) and (22)] are presented in Fig. 16. The stretching $A_1$ and $F_2$ vibrations (solid and open circles) show the same features as in Fig. 15, while $F_2$ bending (open diamonds) mainly contributes in the region around 19 THz and at the top of the lower frequency band (27 THz). The $E$ bending (solid diamonds) exhibits a narrower peak at 15 THz as compared to the peak at 12 THz in Fig. 15. The rotational motion of $SiO_4$ units (crosses) is the most important for eigenmodes around 7 THz.

#### *3. Projection onto vibrations of O-Si-O structural units*

Vitreous silica can also be considered as being comprised of O-Si-O units. A projection analysis for these units has been performed similarly to that for Si-O-Si units (see Sec. V D 1). The results for the partial VDOS characterizing the averaged squared projections of the renormalized eigenvectors onto symmetry modes are given in Fig. 17 and can be compared to Fig. 13. The most essential difference occurs in the lower-frequency band, where the rotations of O-Si-O units (the dotted line in Fig. 17) play the most important role as compared to bending. This is a consequence of the rigidity of the O-Si-O angle in comparison with the quite flexible Si-O-Si angle.

### E. Projections onto coupled rotations

It follows from the above analysis that the rotational motion of all the structural units analyzed is important at low frequencies. In trying to explain the nature of low-frequency vibrations, Buchenau *et al.*[5] proposed a model of coupled rotations of $SiO_4$ tetrahedra. These coupled rotations of a restricted number of tetrahedra (e.g., 5) could be responsible for the low-frquency modes in the boson-peak region. To verify this suggestion, we have projected the eigenvectors onto coupled-rotation modes with the aim of searching for an appreciable enhancement in the values of the squared projections at the lowest frequencies.

The coupled-rotation mode has been constructed in the following way. Consider rotating an $SiO_4$ tetrahedron

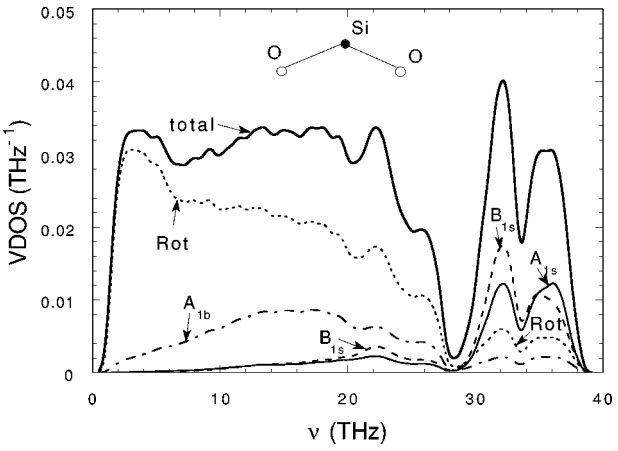


FIG. 17. The partial VDOS's for the projections onto the vibrations of O-Si-O structural units: $A_1$ stretching (the gray solid line), $B_1$ stretching (the dashed line), $A_1$ bending (the dot-dashed line), solid-unit rotations (the dotted line), and their sum (the black solid line) coinciding with the total VDOS.

around random axes passing through the central immobile silicon atom $i$. The vector $\mathbf{a}$ characterizes the displacement of one ($i_0$) of the oxygen atoms (see the inset in Fig. 18). The motion of atom $i_0$ causes the coupled motion of the attached tetrahedron with the Si atom $i'$ at the center. We suppose that this tetrahedron moves as a rigid unit, not changing its shape, i.e., being displaced as a whole in a rotational manner. In order to describe the motion of the attached tetrahedron, we decompose the vector $\mathbf{a}=\mathbf{a}_\parallel+\mathbf{a}_\perp$ into two components which are parallel ($\mathbf{a}_\parallel$) to the bond between atoms $i_0$ and $i'$ and perpendicular ($\mathbf{a}_\perp$) to that bond. All atoms in the attached tetrahedron have the displacement component $\mathbf{a}_\parallel$. The rotational component $\mathbf{a}_\perp$ induces a rotation of the attached tetrahedron around an axis passing through the atom $i'$ and perpendicular to the plane formed by the bond between atoms $i_0$ and $i'$ and the vector $\mathbf{a}_\perp$, thus providing the three other oxygen atoms with the proper rotational displacement vectors $\mathbf{a}^{(r)}_{i''}$. The oxygen atoms (except $i_0$) can also rotate around the bond connecting atoms $i_0$ and $i'$. The amplitude of this rotation is a free parameter for the coupled-rotation mode (the results presented below are practically independent of this parameter).

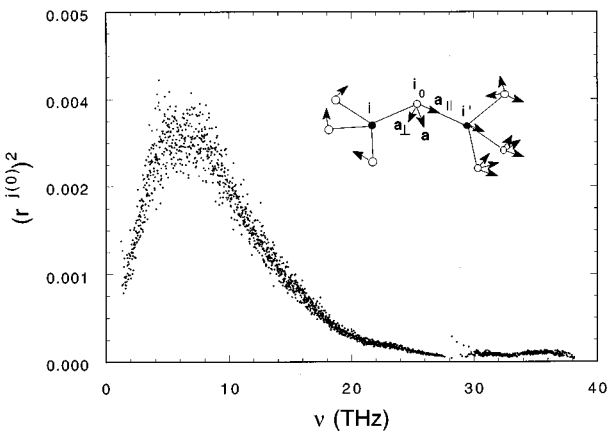


FIG. 18. The squared nonweighted projections of the eigenvectors onto coupled rotations of $SiO_4$ tetrahedra. The atomic displacements for the coupled rotational motion of two connected $SiO_4$ units are shown schematically in the inset.

Following this approach, we attached three more tetrahedra and constructed the coupled-rotation mode involving 21 atoms (or 5 coupled tetrahedra). Then we projected the actual vibrational eigenvectors onto such modes and averaged them over all silicon atoms $i$ at the origin of the central tetrahedron using Eqs. (21)–(23) with $n=0$, where the relative displacement vector $\mathbf{u}^j_{(0)}$ was used instead of $\mathbf{u}^j$. The results of the averaged squared projection of the eigenvectors onto coupled-rotation modes are shown in Fig. 18. These data practically coincide with those for projections onto noncoupled rotations presented in Fig. 16. This means that, on the basis of this analysis, essentially all rotations are coupled to each other. However, it is likely, in fact, that the rotations are coupled together. Our analysis may miss this behavior, since we do not search for the unique axis of coupled rotations, but instead perform an average over all angles for which the contribution from coupled rotations may reduce effectively to zero.

### F. Rigid-unit modes

Structural phase transitions in quartz and $\beta$-cristobalite can be described using rigid-unit modes.[63] Rigid-unit modes represent the collective motion of all atoms which does not cause changes in the shape of $SiO_4$ tetrahedra but influences their mutual orientation. These modes have comparatively low energies (only bond bending around oxygen atoms is involved) and consequently could be supposed to be responsible for the excess modes in the low-frequency (BP) region.[25] We made an attempt to find rigid-unit modes in our model structures of vitreous silica by calculating the averaged relative changes of the volume of $SiO_4$ tetrahedra. The volume $V^j_i$ of an $SiO_4$ tetrahedron with an Si atom $i$ in the center changes (relative to its initial value $V^{(0)}_i$ for the equilibrium static structure) because of the atomic motion. This volume can be represented as a sum of the volumes $V_{i\alpha}$ of four smaller tetrahedra with a common Si atom $i$ at the apex (see inset in Fig. 19), $V^j_i=\Sigma^4_{\alpha=1}V^j_{i\alpha}$. In the rigid-unit mode, the shape of a tetrahedron should not be changed, so that the relative changes in volumes, $\delta V^j_{i\alpha}$, of each small tetrahedron constituting an $SiO_4$ tetrahedron, $\delta V^j_{i\alpha}=(V^j_{i\alpha}-V^{(0)}_{i\alpha})/V^{(0)}_{i\alpha}$ should approach zero for the rigid-unit mode. We plot the weighted ($n=2$) averaged relative changes in the volume of $SiO_4$ tetrahedra $\delta V^{j(n)}$ against frequency in Fig. 19, where

$$\delta V^{j(n)}=\frac{1}{\Sigma_i (w^j_i)^n}\sum_i (w^j_i)^n \sum_\alpha |\delta V^j_{i\alpha}|, \tag{35}$$

with the weight $w^j_i$ defined in Eq. (23). In Eq. (35), we sum the absolute values of the relative changes in order not to take into account modes that change the shape of a tetrahedron but conserve its total volume. As seen in Fig. 19, $\delta V^{j(n)}$ decreases monotonically with decreasing frequency and shows no abrupt decrease (expected if rigid-unit modes exist) in the low-frequency region. Excess modes in the BP region, therefore, cannot be associated with rigid-unit modes in our structural model.

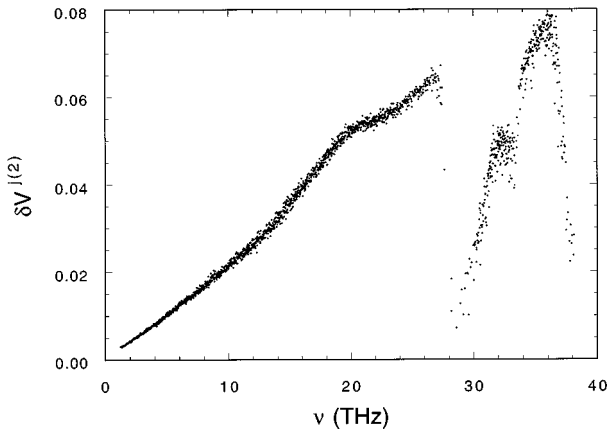


FIG. 19. The weighted [$n=2$ in Eq. (35)] averaged relative changes in volume of $SiO_4$ tetrahedra involved in a particular eigenmode vs the eigenmode frequency.

### G. Vibrational spectrum of small structural units as representative of the spectrum of the entire system

We consider a system of finite size containing quite a large number of atoms. For a system of such size, the main features of the vibrational spectrum (VDOS) are found to be independent of the number of particles, except in the region of the lowest frequencies where acousticlike waves form the spectrum. The very-low-frequency region of the spectrum can be investigated by constructing and analyzing essentially larger systems, and this is not the subject of our consideration. The question we answer in this subsection is whether or not it is possible to describe the main features of the vibrational spectrum of the entire system by investigating the vibrations of small structural units. In other words, what is the most representative of the small structural units in giving the vibrational properties of the entire system?

In order to answer these questions, we have performed a vibrational analysis for our systems using different approximations in the evaluation of the dynamical matrix. Namely, small blocks in the dynamical matrix corresponding to appropriate structural units (clusters of atoms) were considered separately, i.e., extracted from the true dynamical matrix, and the resulting effective dynamical matrix was then diagonalized. The resulting vibrational spectrum obtained for definite structural units can help in understanding the origin of particular features in the total VDOS and reveal the importance of ''interactions'' between atoms in such definite structural units.

First, we considered a small structural unit (e.g., an $SiO_4$ tetrahedron) and calculated its dynamical matrix, evaluating properly the self-interaction matrix elements (i.e., $\sim \partial^2 V/\partial x_{\alpha,i}\partial x_{\beta,i}$, $\alpha$ standing for the Cartesian coordinates) for all atoms $i$ comprising the unit and taking into account only ''interactions'' ($\sim \partial^2 V/\partial x_{\alpha,i}\partial x_{\beta,i'}$) between different atoms $i$ and $i'$ within the unit. Then, the size of the unit was increased by taking into account the second (and third, fourth, or fifth) neighbors to the central atom in the unit. The eigenvalues of these dynamical matrices have been found and averaged over all atoms (being the central atoms in the units) in the whole model and the corresponding VDOS have been obtained.

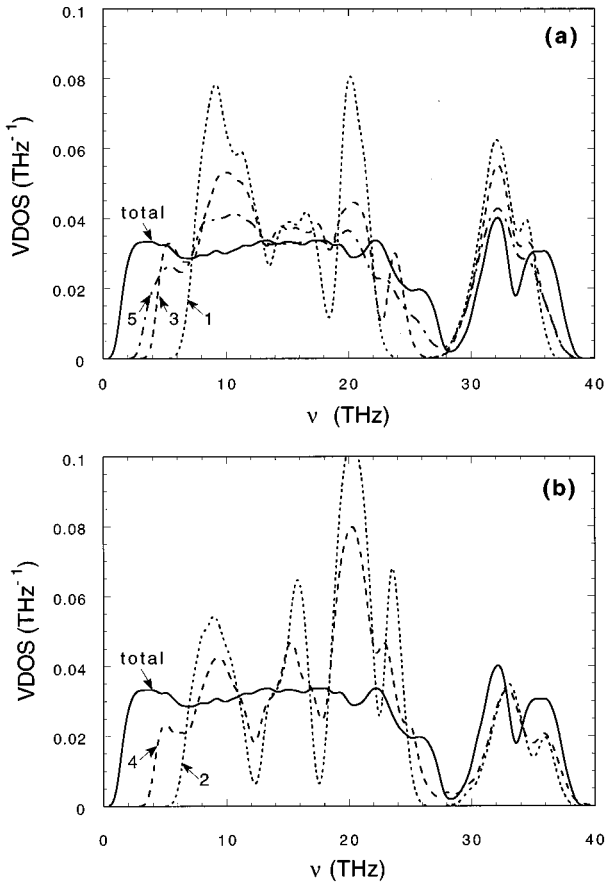


FIG. 20. The VDOS for structural units with silicon atoms as the origin and their $n$th nearest neighbors: (a) first ($n=1$) neighbors (the dotted line), third ($n=3$) neighbors (the dashed line), and fifth ($n=5$) neighbors (the dot-dashed line); (b) second ($n=2$) neighbors (the dotted line) and fourth ($n=4$) neighbors (the dashed line). The VDOS of the entire system obtained in our simulations is represented by the solid line.

The VDOS for the units comprised of the silicon atom and its first, third, and fifth neighbors are shown in Fig. 20(a) while those for the units comprised of the silicon atom and its second and fourth neighbors are given in Fig. 20(b). The analogous VDOS for the structural units containing an oxygen atom at the center are presented in Figs. 21(a) and 21(b). The units containing an odd number of nearest neighbors to a silicon atom actually comprise $SiO_4$ tetrahedra, while the units containing an odd number of nearest neighbors to an oxygen atom comprise Si-O-Si structural units (molecules). A comparison of Figs. 20(a) and 21(a), and especially the curves for the fifth-nearest neighbors, shows that in the case of Si as the origin atom the approximate curve [the dot-dashed line in Fig. 20(a)] fits the calculated VDOS (the solid lines in Figs. 20 and 21) better than in the case of O as the origin atom [the dot-dashed line in Fig. 21(a)]. This means that $SiO_4$ units are better representative structural units than Si-O-Si units. This conclusion agrees with the opinion of the authors of Ref. 6 but contradicts the conclusions of Ref. 19. The units containing an even number of nearest neighbors to a silicon atom comprise an integral number of Si-O-Si units and the partial VDOS in Fig. 20(b) resembles the partial

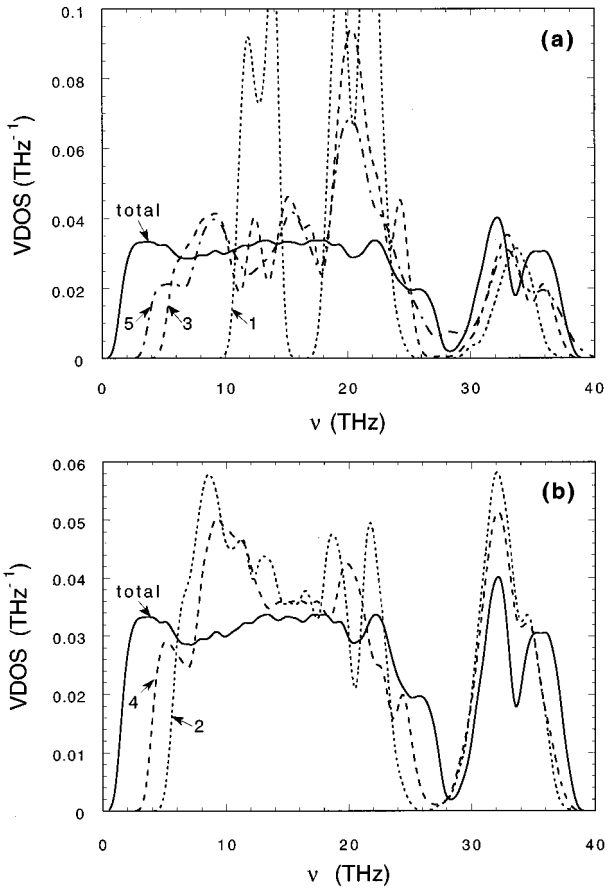


FIG. 21. The VDOS for structural units with oxygen atoms as the origin and their $n$th nearest neighbors: (a) first ($n=1$) neighbors (the dotted line), third ($n=3$) neighbors (the dashed line), and fifth ($n=5$) neighbors (the dot-dashed line); (b) second ($n=2$) neighbors (the dotted line) and fourth ($n=4$) neighbors (the dashed line). The VDOS of the entire system obtained in our simulations is represented by the solid line.

VDOS for O-centered units containing an odd number of nearest neighbors [see Fig. 21(a)] and *vice versa*.

The other important conclusion we can make is that the bottom of the frequency spectrum is shifted to lower frequencies when an increasing number of nearest neighbors is taken into account. Even the inclusion of fifth neighbors (69 atoms with Si as the origin) is not enough to obtain correct frequencies for the low-frequency modes. This means that many atoms (in fact, practically all atoms in the structure, as follows from our projection analysis involving plane waves[55]) are involved in the low-frequency vibrations (in agreement with Ref. 31).

## VI. CONCLUSIONS

We have investigated the vibrational excitations in two structural models of vitreous silica constructed by molecular dynamics. Two of the best, to our knowledge, interatomic potentials (due to van Beest *et al.* and Tsuneyuki *et al.*), based on *ab initio* calculations for a small moleculelike $SiO_4$ unit, have been implemented in the simulations. Both models show good agreement with experimental data with respect to the partial radial distribution functions, the O-Si-O and Si-O-Si bond-angle distributions, and static structure factor. The van Beest model also exhibits a good agreement with experimental data for the dynamical structure factor and fairly good agreement with the vibrational density of states extracted from inelastic neutron scattering. The Tsuneyuki model shows poorer agreement for the dynamical structure factor and the vibrational density of states, mainly due to a shift of the spectrum in the high-frequency region to lower frequencies.

The structural models were relaxed to the equilibrium glassy state and the dynamical matrix was calculated and diagonalized directly, resulting in a complete set of eigenvectors and eigenvalues. Knowing all the eigenvectors, we have investigated the temperature dependence of the mean-square displacement and compared it with the Debye dependence. The experimental value of the mean-square displacement found at $T=50$ K from inelastic and elastic neutron scattering was in good agreement with our calculations.

In the low-frequency region ($\nu\sim 1$ THz), we have found excess (compared to the Debye law) vibrational modes known as the boson peak. The structure and origin of the lowest-frequency modes were briefly discussed and a new model for the states in the boson peak is proposed: The low-frequency states are the transverse acoustic waves strongly overdamped due to hybridization with the states from the bottom part of the lowest optic band (see Ref. 55 for more details). The contributions of these modes to the heat capacity have been investigated and a pronounced bump around $T=20$ K has been found. Unfortunately, we could not investigate the very low-frequency region because of the finite size of our models. Creation of larger models is in progress.

The vibrational analysis performed in order to reveal the nature of vibrational modes included an investigation of the degree of mode localization, phase relations, and mode projections onto the symmetry coordinates of definite structural units. We have found the existence of truly localized states in the high-frequency band tails and quasilocalized states in the low-frequency region. We have also found that the vibrations in the low-frequency range are mainly in phase, resembling acoustic waves, while in the high-frequency range they are mainly out of phase, resembling optic modes. Projections of the modes onto the stretching, bending, and rocking coordinates of oxygen atoms have been made, revealing that stretching is significant only in the high-frequency band, and rocking and bending contribute equally in the low- and medium-frequency range.

Projecting the eigenmodes onto the symmetry coordinates of Si-O-Si, $SiO_4$, and O-Si-O structural units allows us to make a conclusion about the origin of the different features in the VDOS. On the one hand, for Si-O-Si units, $B_1$ stretching (asymmetric) gives dominant contributions to the eigenvectors characterized by frequencies in the region of the two high-frequency peaks in the VDOS at 32 and 37 THz, $A_1$ bending to the states around the top of the lower-frequency band ($\sim$27 THz), and $A_1$ stretching and solid-unit rotations to the peak around 22 THz. On the other hand, for $SiO_4$ units, $A_1$ stretching (asymmetric) contributes only to the eigenvectors characterized by frequencies in the region of the upper peak at 37 THz in the high-frequency band of the VDOS, $F_2$ stretching (asymmetric) appreciably to the two high-frequency peaks in the VDOS at 32 and 37 THz and

slightly to the upper part of the lower band at 22 THz, $F_2$ bending appreciably to the states around the top of the lower-frequency band ($\sim$27 THz) and around 19 THz, $E$ bending to the middle of the lower band around 15 THz, and solid-unit rotations to the bottom part of the lower frequency band at $5-7$ THz. Projecting onto the coupled rotations of $SiO_4$ tetrahedra showed that they play an important role in the same frequency region as noncoupled ones ($\sim 5-7$ THz). No significant enhancement of their contribution in the low-frequency region ($\sim$1 THz) has been found.

We searched for rigid-unit modes, investigating the relative change in the average volume of tetrahedra for different eigenmodes, but found no peculiarities indicative of their presence in the low-frequency region.

We have studied the question of the suitable choice of a small structural unit as being representative of the vibrational properties of the entire system. It was shown that a cluster containing an integral number of $SiO_4$ tetrahedra describes the vibrational properties of vitreous silica better than, at least, a cluster containing an integral number of Si-O-Si structural units. The vibrations of finite-size clusters containing up to 69 atoms do not contribute to the lowest-frequency range $\sim$1 THz.

## ACKNOWLEDGMENTS

We are grateful to the authors of Ref. 26 for sending us unpublished results. One of the authors (S.N.T.) would like to thank Trinity College (Cambridge, UK) for financial support.

[1] S. R. Elliott, *Physics of Amorphous Materials* (Longman, New York, 1990).
[2] A. C. Hannon, M. Arai, R. N. Sinclair, and A. C. Wright, J. Non-Cryst. Solids **150**, 239 (1992).
[3] S. R. Elliott, Phys. Rev. Lett. **67**, 711 (1991).
[4] G. Winterling, Phys. Rev. B **12**, 2432 (1975).
[5] U. Buchenau, H. M. Zhou, N. Nucker, K. S. Gilroy, and W. A. Phillips, Phys. Rev. Lett. **60**, 1318 (1988).
[6] F. L. Galeener, A. J. Leadbetter, and M. W. Stringfellow, Phys. Rev. B **27**, 1052 (1983).
[7] R.O. Pohl, in *Amorphous Solids: Low-Temperature Properties*, edited by W. A. Phillips (Springer-Verlag, Berlin, 1981), p. 27.
[8] A. P. Sokolov, R. Calemczuk, B. Salce, A. Kisliuk, D. Quitmann, and E. Duval, Phys. Rev. Lett. **78**, 2405 (1997).
[9] P. W. Anderson, B. I. Halperin, and C. M. Varma, Philos. Mag. **25**, 1 (1972).
[10] M. I. Klinger, Phys. Rep. **165**, 275 (1988).
[11] R. J. Bell and P. Dean, Philos. Mag. **25**, 1381 (1972).
[12] J. Etchepare and M. Marian, and L. Smetankine, J. Chem. Phys. **60**, 1873 (1974).
[13] T. H. K. Barron, C. C. Huang, and A. Pasternak, J. Phys. C **9**, 3925 (1976).
[14] P. N. Sen and M. F. Thorpe, Phys. Rev. B **15**, 4030 (1977).
[15] L. Guttman and S. M. Rahman, Phys. Rev. B **33**, 1506 (1986).
[16] N. Ahmad, C. M. M. Nex, and W. A. Phillips, Philos. Mag. B **57**, 677 (1988).
[17] R. A. van Santen and R. A. Vogel, Adv. Solid State Chem. **1**, 151 (1989).
[18] A. J. M. de Man, B. W. H. van Beest, M. Leslie, and R. A. van Santen, J. Phys. Chem. **94**, 2524 (1990).
[19] R. B. Laughlin and J. D. Joannopoulos, Phys. Rev. B **16**, 2942 (1977).
[20] K. Mitra, Philos. Mag. B **45**, 529 (1982).
[21] M. J. Sanders, M. Leslie, and C. R. A. Catlow, J. Chem. Soc. Chem. Commun. **1271**, 1984 (1984).
[22] B. Feuston and S. H. Garofalini, J. Chem. Phys. **89**, 5818 (1988); **91**, 564 (1989).
[23] A. Alavi, L. J. Alvarez, S. R. Elliott, and I. R. McDonald, Philos. Mag. B **65**, 489 (1992).
[24] W. Jin, P. Vashishta, R. K. Kalia, and J. P. Rino, Phys. Rev. B **48**, 9359 (1993).
[25] M. T. Dove, M. J. Harris, A. C. Hannon, J. M. Parker, I. P. Swainson, and M. Gambhir, Phys. Rev. Lett. **78**, 1070 (1997).
[26] M. Wilson, P. A. Madden, M. Hemmati, and C. A. Angell, Phys. Rev. Lett. **77**, 4023 (1996).
[27] S. Tsuneyuki, M. Tsukada, H. Aoki, and Y. Matsui, Phys. Rev. Lett. **61**, 869 (1988).
[28] R. G. Della Valle and H. C. Andersen, J. Chem. Phys. **94**, 5056 (1991).
[29] I. P. Swainson and M. T. Dove, Phys. Rev. Lett. **71**, 193 (1993).
[30] R. G. Della Valle and E. Venutti, Chem. Phys. **179**, 411 (1994).
[31] B. Guillot and Y. Guissani, Phys. Rev. Lett. **78**, 2401 (1997).
[32] B. W. H. van Beest, G. J. Kramer, and R. A. van Santen, Phys. Rev. Lett. **64**, 1955 (1990).
[33] K. Vollmayr, W. Kob, and K. Binder, Phys. Rev. B **54**, 15 808 (1996).
[34] S. N. Taraskin and S. R. Elliott, Phys. Rev. B **55**, 117 (1997).
[35] J. Horbach, W. Kob, and K. Binder (unpublished).
[36] J. Sarnthein, A. Pasquarello, and R. Car, Phys. Rev. Lett. **74**, 4682 (1995); Phys. Rev. B **52**, 12 690 (1995).
[37] J. Sarnthein, A. Pasquarello, and R. Car, Science **275**, 1925 (1997).
[38] D. Strauch and B. Dorner, J. Phys.: Condens. Matter **5**, 6149 (1993); H. Schober, D. Strauch, K. Nutzel, and B. Dorner, *ibid.* **5**, 6155 (1993).
[39] Y. Cai and M. F. Thorpe, Phys. Rev. B **40**, 10 535 (1989).
[40] S. H. Garofalini, J. Chem. Phys. **76**, 3189 (1982); J. Non-Cryst. Solids **120**, 1 (1990).
[41] W. Smith and T. R. Forester, J. Mol. Graph. **14**, 136 (1996).
[42] Y. Guissani and B. Guillot, J. Chem. Phys. **104**, 7633 (1996).
[43] C. A. Angell, J. Chem. Phys. **49**, 863 (1988).
[44] D. I. Grimley, A. C. Wright, and R. N. Sinclair, J. Non-Cryst. Solids **119**, 49 (1990).
[45] J. Neuefeind and K.-D. Liss, Ber. Bunsenges. Phys. Chem. **100**, 1341 (1996).
[46] K. Sköld and D. L. Price, *Neutron Scattering* (Academic, New York, 1986).
[47] A. A. Maradudin, E. W. Montroll, G. H. Weiss, and I. P. Ipatova, *Theory of Lattice Dynamics in the Harmonic Approximation* (Academic, New York, 1971).
[48] N. F. Mott and E. A. Davis, *Electronic Processes in Non-Crystalline Materials* (Clarendon, Oxford, 1979).
[49] F. D. M. Haldane, Phys. Rev. B **15**, 281 (1977).
[50] M. Arai, A. C. Hannon, A. D. Taylor, T. Otomo, A. C. Wright, R.

N. Sinclair, and D. L. Price, Trans. Am. Crystallogr. Assoc. **27**, 113 (1991).
[51] D. L. Price and J. M. Carpenter, J. Non-Cryst. Solids **92**, 153 (1987).
[52] F. Terki, C. Levelut, M. Boissier, and J. Pelous, Phys. Rev. B **53**, 2411 (1996).
[53] P. Benassi, M. Krisch, C. Masciovecchio, V. Mazzacurati, G. Monaco, G. Ruocco, F. Settle, and R. Verbeni, Phys. Rev. Lett. **77**, 3835 (1996).
[54] S. R. Elliott, Europhys. Lett. **19**, 201 (1992).
[55] S. N. Taraskin and S. R. Elliott, Europhys. Lett. **39**, 37 (1997).
[56] V. G. Karpov, M. I. Klinger, and F. N. Ignat'ev, Zh. Éksp. Teor. Fiz. **84**, 760 (1983) [Sov. Phys. JETP **57**, 439 (1983)]; B. B. Laird and H. R. Schober, Phys. Rev. Lett. **66**, 636 (1991).
[57] V. L. Gurevich, D. A. Parshin, J. Pelous, and H. R. Schober, Phys. Rev. B **48**, 16 318 (1993).
[58] J. Hafner and M. Crajci, J. Phys.: Condens. Matter **6**, 4631 (1994).
[59] W. Schirmacher and M. Wagener, *Dynamics of Disordered Materials* (Springer, Heidelberg, 1989), p. 231.
[60] S. Alexander and R. Orbach, J. Phys. (France) Lett. **43**, L625 (1982).
[61] H. Bilz and W. Kress, *Phonon Dispersion Relations in Insulators* (Springer-Verlag, Berlin, 1979).
[62] J. C. Decius and R. M. Hexter, *Molecular Vibrations in Crystals* (McGraw-Hill, New York, 1977), p. 64.
[63] F. S. Tautz, V. Heine, M. T. Dove, and X. Chen, Phys. Chem. Miner. **18**, 326 (1991).